

Crustal strain-dependent serpentinisation in the Porcupine Basin, offshore Ireland

Manel Prada (1)*, Louise Watremez (2)**, Chen Chen (2), Brian M. O'Reilly (1), Tim A. Minshull (2), Tim J. Reston (3), Patrick M. Shannon (4), Dirk Klaeschen (5), Gerlind Wagner (5), Viola Gaw (5)

(1) Geophysics Section, Dublin Institute of Advanced Studies, Dublin, Ireland

(2) Ocean and Earth Science, National Oceanography Centre Southampton, University of Southampton, Southampton, UK

(3) School of Geography, Earth and Environmental Sciences, University of Birmingham, Birmingham, UK

(4) School of Earth Sciences, University College Dublin, Dublin, Ireland

(5) Geomar Helmholtz Centre for Ocean Research, Kiel, Germany

*mprada@cp.dias.ie

** now at UPMC, Univ. Paris 6, Sorbonne Universités, IStEP, Paris, France

ABSTRACT

Mantle hydration (serpentinisation) at magma-poor rifted margins is thought to play a key role in controlling the kinematics of low-angle faults and thus, hyperextension and crustal breakup. However, because geophysical data principally provide observations of the final structure of a margin, little is known about the evolution of serpentinisation and how this governs tectonics during hyperextension. Here we present new observational evidence on how crustal strain-dependent serpentinisation influences hyperextension from rifting to possible crustal breakup along the axis of the Porcupine Basin, offshore Ireland. We present three new P-wave seismic velocity models that show the seismic structure of the uppermost lithosphere and the geometry of the Moho across and along the basin axis. We use neighbouring seismic reflection lines to our tomographic models to estimate crustal stretching (β_c) of ~ 2.5 in the north at 52.5° N and > 10 in the south at 51.7° N. These values suggest that no crustal embrittlement occurred in the northernmost region, and that rifting may have progressed to crustal breakup in the southern part of the study area. We observed a decrease in mantle velocities across the basin axis from east to west. These variations occur in a region where β_c is within the range at which crustal embrittlement and serpentinisation are possible (β_c 3-4). Across the basin axis, the lowest seismic velocity in the mantle spatially coincides with the maximum amount of crustal faulting, indicating fault-controlled mantle hydration. Mantle velocities also suggest that

32 the degree of serpentinisation, together with the amount of crustal faulting, increases southwards
33 along the basin axis. Seismic reflection lines show a major detachment fault surface that grows
34 southwards along the basin axis and is only visible where the inferred degree of serpentinisation is >
35 15 %. This observation is consistent with laboratory measurements that show that at this degree of
36 serpentinisation, mantle rocks are sufficiently weak to allow low-angle normal faulting. Based on
37 these results, we propose two alternative formation models for the Porcupine Basin. The first involves
38 a northward propagation of the hyperextension processes, while the second model suggests higher
39 extension rates in the centre of the basin than in the north. Both scenarios postulate that the amount
40 of crustal strain determines the extent and degree of serpentinisation, which eventually controls the
41 development of detachments faults with advanced stretching.

42

43 1 Introduction

44 Serpentinisation is a metasomatic reaction of ultramafic rocks that lowers both the seismic velocity
45 and density of the original rock [e.g., *Carlson and Miller, 2003; Christensen, 2004*], causing
46 volumetric expansion and cracking [*O’Hanley, 1992; Tutolo et al, 2015*]. At rifted margins, this
47 process may occur when crustal-scale faulting takes place, allowing inflow of seawater into the
48 mantle [e.g. *O’Reilly et al., 1996*]. Numerical simulations show that crustal-scale faulting and
49 serpentinisation can occur when the entire crust becomes brittle at a critical stretching factor of 3-4
50 as long as the rift retains low temperatures ($< 600^{\circ}\text{C}$) [*Pérez-Gussinyé and Reston 2001; Guillot et*
51 *al., 2015*], which makes serpentinisation a widely recognised process of magma-poor rifted margins.

52 As inferred from seismic velocity models [*Bayrakci et al., 2016*], serpentinisation at magma-poor
53 rifted margins is not only controlled by the occurrence of crustal-scale faulting but also by total fault
54 displacement. This observation suggests that water can only effectively infiltrate the mantle during
55 the late syn-rift stage when normal faults are still active [*O’Reilly et al., 1996*]. Serpentinisation has
56 important tectonic implications since it reduces the friction coefficient of mantle rocks [*Escartín et*
57 *al., 2001*], and causes the formation of secondary minerals that, along with reaction-driven fracturing
58 [*Tutolo et al, 2015*], causes high fluid pressure [*Moore et al., 1996*]. Weakening of mantle rocks and
59 fluid overpressure are both proposed to have a critical role in the kinematics of low-angle faults like
60 the S detachment along the Galicia Margin [*Reston et al., 2007*]. Additionally, thermo-mechanical
61 simulations based on geophysical and geological observations suggest that the formation of weak
62 regions in the lithosphere causes rift acceleration [*Huisman and Beaumont, 2003; Brune et al.,*
63 *2016*], which is critical in shaping rifted margins as it controls their asymmetry [*Huisman and*
64 *Beaumont, 2003; Brune et al., 2014*]. Hence, understanding the evolution of serpentinisation and its
65 role in controlling tectonic processes at magma-poor rifted margins will provide new insights into the
66 formation of continental passive margins. However, very little is known regarding the evolution of
67 mantle hydration with progressive lithospheric extension. This is because most of the observations
68 are made along mature rifted margins, in which the mantle is already exhumed and seafloor spreading
69 is established [e.g. *Whitmarsh et al., 1996; Funk et al., 2003; Davy et al., 2016*].

70 In this work, we focus on the Porcupine Basin, a north-south triangular-shaped basin located in the
71 North Atlantic margin southwest of Ireland (Fig. 1a). The Porcupine Basin is a failed rift in which
72 extension increases dramatically from north to south along the basin axis [*Tate et al., 1993; Watremez*
73 *et al., 2016*]. This increase makes the Porcupine Basin an ideal natural laboratory to assess the
74 variations of formation processes related to progressive lithospheric stretching. We present a set of
75 P-wave seismic velocity (V_p) models derived from travel time tomography of wide-angle seismic
76 (WAS) data acquired in the Porcupine Basin (Fig. 1a). The models reveal the seismic structure of the

crust and uppermost mantle, as well as the geometry of the Moho across and along the basin axis from the northern ($\sim 52.5^\circ$ N) and less extended region of the basin, to the central region ($\sim 51.5^\circ$ N), where hyperextension occurred due to advanced tectonic stretching [e.g. Reston et al., 2001, 2004]. Careful analysis of uppermost mantle V_p from our models suggest along- and across-axis variations in mantle hydration. We use gravity data and seismic reflection profiles near our V_p models to explore potential reasons for such variations, and assess their implications for the formation of the Porcupine Basin.

2 Tectonic setting

The Porcupine Basin was formed in response to several rift and subsidence phases during the Late Paleozoic and Cenozoic, with the most pronounced rift phase occurring in Late Jurassic–Early Cretaceous times [Tate et al., 1993; Naylor and Shannon, 2011]. Subsidence curves [Tate et al., 1993] suggest that axial stretching factors (i.e., $\beta_c = T_0/T_1$; T_0 is initial crustal thickness before extension, and T_1 the current crustal thickness) increase from 1.5–2 in the north to 3–4 in the central region. However, WAS data [Watremez et al., 2016] and seismic reflection data [Reston et al., 2004] both show that maximum β_c are at least 3 and 2 times greater than these estimates in the northern and central parts of the basin, respectively. This discrepancy can be explained by mantle serpentinisation, which reduces the density of mantle rocks, and therefore reduces the effect of thermal subsidence. A similar effect is inferred from seismic data in the Rockall Basin, northwest of the Porcupine Basin in the North Atlantic [O'Reilly et al., 1996].

Mantle hydration in the Porcupine has been proposed by many authors based on geophysical data [Reston et al., 2001, Readman et al., 2005; O'Reilly et al., 2006; Watremez et al., 2016]. Gravity data reveal a major positive free air gravity anomaly between 51.5° – 52.5° N (Fig. 1b) that suggests the presence of extremely thin crust and a low density uppermost mantle (i.e., < 3.3 g/cm³). This anomaly is also associated with a major tectonic feature known as the Porcupine Arch [Naylor et al., 2002], recognised on seismic reflection profiles as a deep, bright and continuous package of high-amplitude reflectivity [Johnson et al., 2001; Reston et al., 2001; Naylor et al., 2002]. The Porcupine Arch was previously interpreted either as the top of the crystalline crust [Johnson et al., 2001; Naylor et al., 2002], or as a detachment surface (i.e., the P-detachment) representing the Moho (i.e. crust-mantle boundary) [Reston et al., 2001, 2004]. WAS data modelling has revealed V_p between 7.5 and 8 km/s below the Porcupine Arch [O'Reilly et al., 2006; Watremez et al., 2016], which is too high for continental crust but not for serpentinised mantle rocks [Carlson and Miller, 2003]. This result not only supports the hypothesis that the Porcupine Arch is the Moho, but also suggests that the mantle below is partially serpentinised [i.e. ~ 10 – 20% ; O'Reilly et al., 2006]. Interestingly, Reston et al.

110 [2001, 2004] noted the presence of major faults crosscutting the entire syn- and pre-rift section up to
111 the top of the Arch, implying that crustal embrittlement has occurred in the Porcupine Basin, further
112 supporting the hypothesis of a serpentinised mantle.

113 3 Wide-angle seismic data analysis and modelling

114 In 2004, three WAS profiles were collected along pre-existing reflection profiles across the Porcupine
115 Basin [Reston et al., 2001, 2004] (Fig. 1a). Up to 24 four-component ocean-bottom seismometers
116 (OBS) and ocean-bottom hydrophones (OBH) were used to acquire the data along each of the three
117 lines presented here (Fig. 1a). The receivers were spaced every ~8 km along each line and the seismic
118 source was generated by 2-3 32 litre (2000 in³) airguns fired every 60 s (~120 m).

119 Seismic refraction data processing involved a predictive deconvolution and a bandpass filter defined
120 by frequencies of 1-5-15-25 Hz. The data show clear refraction and reflection travel times
121 corresponding to the sedimentary section, the crystalline basement and the uppermost mantle (Fig.
122 2). In particular, the data show a prominent phase at large offsets with apparent velocity of 8 km/s
123 that has been interpreted as a refracted phase through the uppermost mantle or P_n (e.g., >40 km model
124 offset in Figs. 2 and 3d). A high-amplitude reflection identified at shorter offset than P_n arrivals has
125 been interpreted as the critical reflection at the Moho or P_mP (Figs. 2 and 3). Overall, we manually
126 picked a total of 28,995 travel times of refracted and reflected phases for line P02, 31,676 for line
127 P03, and 35,708 for line P04. Picking uncertainties were automatically assigned between 20 and 125
128 ms based on the signal to noise ratio of the trace 250 ms before and after the picked arrival time,
129 following the empirical relationship of Zelt & Forsyth (1994).

130 The data were inverted for V_p structure and geometry of seismic interfaces (e.g., Moho) using the
131 method of Korenaga et al. [2000]. This method computes the travel time residuals by calculating the
132 shortest ray-path for each travel time, and solves a linearized inversion problem to minimise the travel
133 time residuals. The V_p models were obtained following a layer stripping strategy [e.g. Sallarès et al.,
134 2011], so that refracted and reflected travel times of each layer were inverted sequentially from near
135 to far offset, resolving at each step the velocity and depth of each layer of the model from the shallow
136 sediments to the uppermost mantle. Travel times of critical reflections at sedimentary interfaces were
137 identified in all the lines (Figs. 2 and A1), and included in the layer stripping (see Fig. A2 for layer
138 stripping sequence of each model). However, given that the main goal of the study relies on the deep
139 structure of the basin, we only show the geometry of the Moho interface (blue thick lines in Fig. 4).
140 The grid spacing for P04 was optimally set at 0.25 x 0.25 km, whereas for P03 and P02 it varies
141 vertically from 0.1 km at the top to 0.5 km at the bottom, and it was held constant horizontally along
142 the grid at 0.3 km. The finer grid spacing at shallow levels along dip lines P03 and P02 was designed

to allow for seismic heterogeneity caused by sedimentary structures associated to the margins of the basin. The grid spacings chosen are much smaller than the anomaly size (i.e. >10 km wide) that we can retrieve at the depths of interest (i.e. ~15 depth). Thus, these grids are optimum for the purpose of the study.

Regularization parameters are defined by a set of horizontal and vertical correlation lengths that vary from top to bottom in the grid. Horizontal correlation lengths (HCL) were 3 km at the top of all models and increased to 10-12 km at the bottom of the grid. Vertical correlation length (VCL) was 0.2-0.5 km at the top of the grid and 5-8 km at the bottom of the grid. Reflector correlation lengths (RCL) were set at 4 km and the depth kernel-scaling factor (W) was 0.1-0.5. Overall, tomographic models in Fig. 4 have a good data fit as root mean square of residual travel times are around half of the dominant wavelength (i.e. 20-30 ms for sediment phases, and ~50ms and ~80ms for crustal and mantle phases, respectively; see Tables A1 to A3 for further details of root mean square values).

3.1 Model parameter uncertainty

The range of uncertainty values of V_p and depth of the Moho was assessed by means of a Monte-Carlo analysis. The approach was performed for each of the different layers following the same layer-stripping strategy applied for the inversion of the preferred models in Fig. 4. In this case, for each layer, we produced 100 realisations (120 for line P04). Each realisation consisted in a travel-time dataset with added random noise (up to ± 125 ms), an input model for the corresponding layer with a random 1D velocity-depth distribution ($\pm 10\%$ and $\pm 6\%$ for crustal and mantle velocities, respectively), and a flat reflector with a random depth (± 4 km for the Moho). HCL, VCL, RCL and W were also randomised during the Monte-Carlo analysis (HCL 5 ± 2 km and 15 ± 5 km and VCL 0.5 ± 0.2 km and 6 ± 2 km at the top and bottom of the model, respectively; RCL 5 ± 1 km; W between ~0.1 and ~1). This process allowed us to assess the optimum range of regularization parameters, which resembles the range used to obtain the preferred models of Fig. 4. The standard deviation of the inverted 100 models (120 for line P04) was computed and taken as a statistical measure of the uncertainty of the model parameters [Tarantola, 1987; Korenaga et al., 2000] (Fig. 5).

Overall, the V_p structure of the three models is well constrained in areas with a good ray coverage (see Fig. A3 for ray coverage information). The standard deviation (i.e., statistical uncertainty) of velocities in lines P02 and P03 ranges between 0.1 and 0.3 km/s (Fig. 5), whereas it is < 0.2 km/s for line P04 (Fig. 5). In particular, uppermost mantle velocities are generally well constrained with values < ± 0.2 km/s, except along line P02 where locally they reach $\sim \pm 0.3$ km/s (Fig. 5). Higher uncertainties along P02 are the result of combining a high pick uncertainty (i.e. ~125 ms) of P_n phases with a lower ray coverage in that particular area of the model (i.e. between 120 and 140 along P02 Figs. 5 and A3). The Moho depth is well constrained in the centre of the models with uncertainties < ± 0.2 km (Fig. 5),

177 whereas it is less constrained towards the edges of the model given the lack of P_mP arrivals (see Fig.
178 A4 for ray tracing of P_mP arrivals).

179 4 Results

180 The northernmost W-E profile P03 runs across the northern Porcupine Basin and shows a sedimentary
181 basin fill displaying V_p between 1.5 and 4.0-4.5 km/s that thickens towards the centre of the basin,
182 reaching 8-9 km thick [Watremez et al., 2016]. Syn-rift sediments are represented by V_p between 4.5
183 and 5.0 km/s and basement velocities range from 5.0-5.5 to 6.6-6.8 km/s, that is typical for crystalline
184 continental crust [Christensen & Mooney, 1995] (Fig. 4). The Moho obtained from inversion of P_mP
185 arrivals shallows to 15 km depth at ~ 130 km of profile distance (Fig. 4a). Below this thinnest section
186 of the crust (km 115-145), the uppermost mantle V_p is not only slower than unaltered peridotite (i.e.,
187 8.0 km/s), in agreement with previous studies [O'Reilly et al., 2006], but also decreases by 0.4 km/s
188 from east to west, from ~8.0 to ~7.6 km/s (Fig. 6a).

189 The southernmost dip line P02 is located in the southern region of the study area (Fig. 1), and shows
190 a similar sedimentary cover with V_p between 1.5 and 4.0-4.5 km/s that can be up to ~8 km thick.
191 Basement velocities in the margins are similar to P03, ranging from 5.0-5.5 to 6.6-6.8 km/s, but they
192 barely exceed 6.0 km/s in the basin centre, where the crust is thinnest (e.g. between 120 and 150 km
193 of profile distance in Fig. 4c). From the neighbouring reflection line 106 (Fig. 7), we observe that
194 crustal $V_p < 6.0$ km/s spatially coincides with a pervasively faulted sequence (e.g. between 120-150
195 km of profile distance in Fig. 7a), which appears to comprise both basement and highly rotated syn-
196 rift sediments [Reston et al., 2004]. The P_mP -derived Moho along P02 shallows up to ~11 km depth
197 (Fig. 4c), that is 2 km shallower than the Moho along P03, indicating that extension increases
198 southwards along the basin axis. Mantle velocities are slower than those of pristine mantle rock and
199 are characterised by strong lateral variations, similar to P03. In this case, however, V_p decreases up
200 to 1 km/s from east to west, from 8.0-8.2 to 7.0-7.2 km/s (Fig 6b).

201 The N-S line P04 runs along the basin axis crossing profiles P03 and P02 (Fig 1 and 4). The
202 sedimentary cover with V_p between 1.5 and 4.0-4.5 km/s, previously imaged by P03 and P02 across
203 the basin axis, is also imaged along the basin axis thinning subtly from north to south ~1-2 km (Fig.
204 4a). Beneath this, crustal V_p increases with depth from 5.0-5.5 to 6.4-6.6 km/s (Fig. 4a). The resolved
205 Moho shallows from 20 km deep in the north to ~11 km in the south, which denotes again a significant
206 crustal thinning from north to south along the basin axis (Fig. 4a). In agreement with the rest of the
207 profiles, velocities in the uppermost mantle are slower than 8.0 km/s. However, no significant
208 variations of mantle velocities are observed along the profile except at km 110, where mantle V_p
209 increases gently in the uppermost section of the mantle, from north to south (Fig. 4a).

210 5 Discussion

211 5.1 Variations of mantle hydration across the basin axis

212 The tomographic results along dip lines show across-axis variations in uppermost mantle V_p (Figs. 6a
213 and 6b). In both cases, seismic velocities increase towards the east where seismic velocity can be up
214 to 1 km/s faster (i.e., case for P02, Fig. 6b). Comparing the vertical seismic structure of W-E lines
215 P03 and P02 with N-S line P04 at the corresponding intersection points (Figs. 6c and 6d), we observe
216 small differences that are within the velocity error (i.e. up to 0.2 km/s in Figs. 6c and 6d). Hence, we
217 cannot conclude whether these small variations are due to variations in model parametrization, to data
218 uncertainties, or to anisotropy. If anisotropy was the main contributor to such variations, its effect is
219 still too small to explain across-axis velocity variations in the uppermost mantle (i.e. Figs. 6a and 6b).

220 Anisotropy is suggested to be caused by alignment of cracks, damage zones and serpentinisation
221 within fault zones in the outer rise of subduction zones (with the slowest propagation perpendicular
222 to fault zone) [Miller and Lizarralde, 2016]. However, the faulting responsible for mantle hydration
223 in this setting [i.e. bending-related faulting; Ranero *et al.*, 2003] is closer to the vertical than that
224 responsible for extension in the Porcupine [Reston *et al.*, 2004]. Hence, the small discrepancy of
225 seismic wave speed between W-E and N-S propagation in the Porcupine Basin may be explained by
226 the low-angle orientation of damage zones in the W-E direction (the approximate direction of
227 extension). This orientation would result in a similar propagation of refracted seismic waves (i.e.
228 subhorizontal propagation) in both W-E and N-S directions, and reduce azimuthal anisotropy caused
229 by alignment of damage zones. Hence, variations of mantle V_p across the basin axis potentially reflect
230 petrological variations, which in this case may indicate differences in the degree of magmatic
231 intrusion and/or serpentinisation.

232 Geological observations from boreholes [Tate & Dobson, 1988], coupled with seismic stratigraphic
233 interpretation [Reston *et al.*, 2004], suggest that there was little syn-rift magmatism in the northern
234 and southern region of the study area (i.e. 51.5° to ~53° N; Fig. 1). Sills intruded in the post-rift
235 sequence at ~60-61 Ma (i.e., early Paleocene) indicate the first major magmatic activity [Tate &
236 Dobson, 1988]. As observed in other regions in the North Atlantic [e.g., Archer *et al.*, 2005] the
237 intrusion of magmatic bodies after the deposition of post-rift sediments drives significant uplift and
238 consequent deformation of the older post-rift sequence (mostly Cretaceous in our case). However,
239 seismic reflection lines reveal no domal deformation in the Cretaceous unit (Fig. 7a) that could be
240 attributed to such effects. Instead, a flat and undeformed post-rift sequence is observed, suggesting
241 that early Cenozoic magmatism (crustal intrusion and underplating) is an unlikely explanation for
242 low subcrustal velocity variations.

Alternatively, mantle serpentinisation has been proposed during the formation of the basin [Reston et al., 2001, 2004; Readman et al., 2005; O'Reilly et al., 2006]. Numerical modelling of evolving rheology and temperature [Pérez-Gussinyé and Reston 2001] predicts that at stretching factors of 3-4 the crust becomes entirely brittle and the subcrustal mantle cools enough (<600°C) to serpentinise at rifting rates appropriate for the Porcupine Basin [Reston et al., 2004], especially in the absence of voluminous syn-rift magmatism [Tate & Dobson, 1988] to advect heat.

The degree of extension in the northern region of the basin has been assessed in Watremez et al. [2016] by combining velocity model P03 with its coincident seismic line Wire2 (Fig. 1). The result of this combination reveals that the minimum crustal thickness along P03 is ~5 km, corresponding to a β_c of ~6 (at ~120 km of profile distance; Fig. 4b), assuming an original crustal thickness of ~30 km SW of Ireland [Lowe & Jacob, 1989; O'Reilly et al., 2010]. This amount of extension is well within the range at which crustal embrittlement is expected [i.e. 3-4 in Pérez-Gussinyé and Reston 2001].

In the south, the comparison between the seismic reflection line 106 and the velocity model along P02 shows that the geometry of the P-detachment resembles the geometry of the WAS-derived Moho (Fig. 7b). Particularly, between km 140 and 155 the WAS-derived Moho follows the base of reflections associated with the Moho according to Reston et al [2001]. However, some discrepancies exist between these two seismic interfaces. Towards the east, between km 155 and 165 (Fig. 7b), the WAS-derived Moho is slightly shallower (i.e. < 0.5 s two-way time) than the eastward-dipping reflections interpreted by Reston et al [2001] as the Moho (Fig. 7). Given that the fault plane of the detachment and the eastward-dipping reflections associated with the Moho are close to each other in this particular area, such discrepancy could be attributed partly by cycle-skipping in P_mP arrival times. Further discrepancy is observed towards the west, between km 135 and 140 (Fig. 7b), where the P-detachment in the reflection is steeper than the tomographically resolved Moho (Fig. 7b). In this case, a single strong impedance contrast is observed in the reflection line, which makes cycle-skipping unlikely. Alternatively, seismic reflection lines (Fig. 7) reveal that the P-detachment flattens rapidly along the basin axis from north to south. Hence, given that line P02 was acquired 5 km south of 106 it is likely that the geometry of the P-detachment varies from line 106 to P02 farther south. Also, the smoothing inherent in the inversion might have contributed to this difference. Regardless of these discrepancies, the wide-angle reflection modelled as the Moho is defined by a significant velocity contrast ($> 1.5 \text{ s}^{-1}$) and it overlies material with $V_p \sim 8 \text{ km/s}$, making this interface an ideal candidate for the Moho. Our results thus support the hypothesis of Reston et al. [2001] that most of the P-detachment forms a tectonic boundary between the crust and the mantle, and that crustal faulting associated with the P-detachment would have facilitated mantle serpentinisation.

276 The combination of the reflection line 106 and model P02 also allows us to provide some estimates
277 of crustal thickness. We infer that the crystalline basement, if any, in the most extended region along
278 line P02 could be as thin as 2 km (i.e., between 140 and 155 km of line P02, Fig. 7), which implies a
279 $\beta_c > 10$. At this degree of extension, rifting could have reached breakup, which means that syn-rift
280 sediments (now exhibiting crustal velocities) could be deposited directly on the mantle in this region
281 of the central Porcupine Basin. This configuration would imply that a substantial part of the rift
282 process has been accompanied by ongoing serpentinisation, which is in agreement with low mantle
283 V_p observed along model P02 (i.e. ~ 7.0 - 7.5 km/s in Fig. 6b).

284 To test V_p from our models and explore the hypothesis of variations in mantle hydration across the
285 Porcupine Basin axis we performed gravity modelling following the method of *Korenaga et al.*
286 [2001]. We tested two possible scenarios: a model with homogenous unaltered mantle, and a model
287 with lateral variations of density in accordance with seismic velocities. This way, V_p from our models
288 was converted to density (ρ) using the V_p - ρ relationships of *Hughes et al. [1998]* for sediments and
289 *Christensen & Mooney [1995]* for the crystalline continental crust. For the mantle, a ρ of 3.3 g/cm^3
290 was assumed for the first scenario, while *Carlson and Miller's [2003]* relationship for serpentinised
291 mantle rocks was used to test the second scenario. The results show that for both lines P02 and P03
292 the best-fitting gravity anomaly is that derived from ρ models of the second scenario, in which
293 densities in the uppermost mantle vary across the basin axis (Fig. 8). These results support V_p
294 obtained from travel time tomography and a heterogeneous hydration of the mantle.

295 We compare the tectonic structure with the velocity field (Fig. 7b) to explore for potential reasons for
296 such variations in mantle hydration. This comparison reveals that crustal faulting in the Porcupine
297 Basin is spatially denser above the lowest mantle V_p (i.e., highest degree of serpentinisation), whereas
298 it is less intense above areas where mantle V_p is higher (i.e., lower degree of serpentinisation) (Fig.
299 7b). This correlation suggests that crustal-scale faulting has controlled mantle hydration in the
300 Porcupine Basin, similar to the Galicia margin, where it has been suggested that water supply to the
301 mantle occurred when faults were active *[Bayrakci et al., 2016]*.

302 5.2 Along axis variations of mantle hydration: implications for the formation of the Porcupine 303 Basin

304 The comparison between dip lines P03 and P02 shows that mantle V_p decreases from north to south
305 in those areas where the inferred degree of mantle hydration is higher along both models (Fig. 9b).
306 This observation suggests a southward increase in the degree of serpentinisation along the basin axis,
307 from 15-20 % to 25-35% (Fig. 9b). Interestingly, seismic reflection lines show that the P-detachment
308 is only visible south of line Wire2 (Fig. 9c) *[Klemper and Hobbs 1991]*, where the inferred degree of
309 hydration is higher than 15% (Fig. 9b). This correlation is consistent with laboratory measurements,

310 which indicate that a 10-15% degree of serpentinisation is needed to reduce significantly the friction
311 coefficient of the original mantle rock, allowing the development of low-angle normal faults
312 [Escartín *et al.*, 2001; Reston *et al.*, 2007].

313 Given the relevance of crustal faulting in controlling mantle hydration, we looked for along-axis
314 variations in crustal faulting. Seismic reflection line Wire2 (Figs. 1 and 9), coincident with line P03,
315 displays the lowest quality at depth of the four seismic reflection lines shown in Fig. 9c as it was
316 acquired with the shortest streamer [*i.e.* 4 km; Klemper and Hobbs 1991]. Hence, crustal faults are
317 poorly imaged in depth compared to line PAD (10 km long streamer), 103 and 106 (6 km long
318 streamer), all acquired with a longer streamer than Wire2 (4 km long streamer). Despite this quality
319 issue, Wire2 clearly images one crustal fault (Fig. 9c) reaching the WAS-derived Moho (blue dashed
320 line in Fig. 9c). Southwards from Wire2, seismic lines PAD, 103 and 106 show the surface of the P
321 detachment (white dots in Fig. 9c), which becomes larger southwards together with the number of
322 seismically resolved crustal faults (red dashed lines in Fig 9c). In particular, the syn-rift section along
323 the southernmost seismic line 106 contains at least seven faults that crosscut the entire section down
324 to the P-detachment. Velocities along P02 are < 6km/s in the lower crust (*i.e.* between km 130 and
325 145 of Fig. 7), which is in agreement with the highest concentration of faulting. Overall, the seismic
326 reflection lines in Fig. 9c show that crustal faulting in the Porcupine Basin increases southwards in
327 agreement with the degree of extension, and mantle hydration.

328 We have compared the V_p -derived degree of serpentinisation from those areas of models P02 and
329 P03 where mantle V_p is lowest and ray coverage is satisfactory (Fig. 10), with the amount of
330 seismically-resolved crustal faulting along their corresponding neighbouring seismic reflection lines
331 (*i.e.*, Wire2 for P03, and 106 for P02). This comparison illustrates the good correlation between the
332 degree of mantle hydration and the number of crust-penetrating normal faults along the basin axis
333 (Fig. 10). However, there is no apparent impedance contrast between the syn- and pre-rift section
334 within half-grabens (Fig. 9c), and no well has been drilled that deep (*i.e.* > 8 km), so we cannot
335 reliably estimate fault displacements. Thus, we cannot assess whether the number of faults or the fault
336 displacement [Bayrakci *et al.*, 2016] is more important in controlling access of water to the uppermost
337 mantle in the Porcupine Basin.

338 Regardless of the displacement of faults, our results provide observational evidence of the
339 development of tectonic features related to progressive stretching and serpentinisation along the axis
340 of the Porcupine Basin. As shown by dip lines P03 and P02, the degree of extension increases
341 southwards. This is better illustrated by model P04 (Fig. 4a), in which a β_c of ~2.5 can be estimated
342 in the northernmost section of the basin - assuming a V_p of ~5.5 km/s as the top of the crystalline
343 basement - increasing to $\beta_c > 10$ in the southern part of the study area (~ 51.7°N). The low degree of

344 extension in the northernmost section of the basin suggests that crustal embrittlement may not have
345 occurred in this region [$\beta_c < 3$; *Pérez-Gussinyé and Reston 2001*]. Thus, based on line P04, the along-
346 axis transition between rifting and potential crustal breakup occurs over a distance of 80 km. Within
347 this transition, the degree of serpentinisation increases towards the south, where it reaches maximum
348 values of ~35-40% (Fig. 10). In addition, as the degree of serpentinisation increases the P-detachment
349 becomes more important as its surface grows southwards (Fig. 7b).

350 Based on these observations, one possible formation model of the basin is that crustal embrittlement
351 and mantle serpentinisation started in the south of our study area. Increased serpentinisation (> 15%)
352 and extension then caused the formation of the P-detachment in the same region, creating a weak spot
353 in the rift. Then, progressive lithospheric stretching allowed the propagation of crustal deformation
354 to the north along the basin axis. As long as crustal faults remained permeable enough to percolate
355 water to the mantle and rift temperatures were $< \sim 600^\circ\text{C}$, serpentinisation and the development of the
356 P-detachment would have also propagated along the basin axis in agreement with the degree of
357 stretching. This scenario implies that hyperextension occurred first in the southern region of our study
358 area and propagated to the north of the basin later.

359 Alternatively, crustal embrittlement, serpentinisation and development of low-angle faults might have
360 occurred contemporaneously along the basin axis. Since the amount of extension increases
361 southwards, more crustal faults would have developed in the centre of the basin than in the north.
362 Thus, more water would have accessed the mantle in the central region than in the north favouring
363 faster serpentinisation and development of detachment faults. This scenario implies that the central
364 region has opened at higher rates than the northern basin. Given the importance of extension rates in
365 controlling partial decompression melting during lithospheric stretching [*Reid and Jackson 1987*;
366 *Pérez-Gussinyé et al., 2006*], this latter scenario could explain the presence of voluminous
367 magmatism in the south Porcupine Basin [*Calves et al., 2012*; *Watremez et al., 2016*]. Thus, we
368 consider this second scenario as our preferred model of the basin formation, as it is compatible with
369 tectonic and inferred magmatic events further south in the Porcupine Basin. However, our data do not
370 allow us to distinguish between both models, as they fail to provide chronological information of the
371 syn-rift sequence related to crustal faulting along the basin axis. Further data (i.e. well and 3D seismic
372 data) are needed in the centre and southern region of the Porcupine Basin to more fully understand
373 the formation of the basin.

374 Overall, despite of their different assumptions regarding the timing of tectonic events, in both models
375 the initial distribution of crustal deformation during rifting controls the location and extent of
376 serpentinisation, which together with the amount of extension, governs the onset and growth of
377 detachment faults, and hence of hyperextension in the Porcupine Basin.

378 6 Conclusions

379 The V_p models presented in this study show the uppermost lithospheric seismic structure and the
380 geometry of the Moho, across and along the Porcupine Basin axis with unprecedented detail. The
381 velocity structure shows an 8-9 km thick post-rift sedimentary blanket with V_p between 1.5 and 4.5
382 km/s. The underlying basement displays V_p between 5.0-5.5 to 6.6-6.8 km/s, except for some areas
383 along P02 where lower crustal velocities are < 6.0 km/s. The combination of seismic reflection line
384 106 and model P02 reveals that $V_p < 6.0$ km/s are associated to a high degree of fracturing.

385 The combination of V_p models with the tectonic structure allows us to estimate β_c along each
386 tomographic model. Our results confirm that the degree of extension increases dramatically
387 southward from $\beta_c \sim 2.5$ in the north of the basin to > 10 in the southern part of the study area ($\sim 51.5^\circ$
388 N). Low β_c values in the north imply that no crustal embrittlement occurred in this region of the
389 Porcupine Basin. Based on these results, the along-axis transition between rifting and potential crustal
390 breakup occurs over an 80 km region in the Porcupine Basin axis.

391 Velocity models also reveal that mantle velocities decrease from east to west up to 1 km/s across the
392 basin axis. These velocities can be explained either by variations in the presence of subcrustal
393 magmatic rocks or mantle serpentinisation. The lack of voluminous syn-rift magmatism in this area
394 of the Porcupine Basin is difficult to reconcile with the first hypothesis, and the presence of major
395 crustal faults spatially coinciding with the lowest subcrustal V_p suggests that faults controlled mantle
396 hydration in the Porcupine Basin.

397 The comparison between P03 in the north and P02 in the south reveals that the degree of
398 serpentinisation increases southwards from 15-20 % to 25-35%. This is consistent with the fact that
399 the P-detachment is only visible south of P03, where the degree of alteration is > 15 %, and hence
400 sufficient for low-angle faulting [*Escartín et al., 2001; Reston et al., 2007*]. Our results show that
401 along-axis variations in the degree of serpentinisation correlate linearly with the number of crustal
402 faults identified along seismic reflection lines.

403 Based on the seismic and tectonic structure of the basin presented here we suggest two likely scenarios
404 of basin formation. The first one postulates that crustal embrittlement, serpentinisation and
405 hyperextension occurred first in the southern region of the study area and then propagated northward.
406 The second scenario proposes that serpentinisation and crustal deformation occurred
407 contemporaneously along the basin axis implying faster rates of extension in the south than in the
408 north. In both scenarios, the original distribution of crustal faulting determines the location and extent
409 of serpentinisation, which eventually governs the kinematics of detachment faults.

Overall, our work presents for the first time observational evidence of crustal strain-dependent serpentinisation in the Porcupine Basin and its implications for the development of tectonic processes related to hyperextension.

413

ACKNOWLEDGMENTS

This project is funded by the Irish Shelf Petroleum Studies Group (ISPSG) of the Irish Petroleum Infrastructure Programme Group 4. Gravity and seismic line PAD was provided by the Petroleum Affairs Division of the Department of Communications, Climate Action and Environment, Ireland. Seismic reflection data SPB97-103/106 were supplied by Fugro-Geoteam through Conoco-Phillips. Wide-angle seismic data collection was funded by the Deutsche Forschungsgemeinschaft through grant Re 873/10 and was enabled by the professionalism and skill of the officers and crew of the FS Meteor during cruise M61-2. Profile Wire2 was acquired during the BIRPS WIRE project, which was funded by the Natural Environment Research Council (UK), the Department of Energy (Ireland) and Western Geophysical. T.A. Minshull was supported by a Wolfson Research Merit award. We would like to acknowledge the Editor John P. Brodholt and two anonymous reviewers for a very thorough review that helped to improve the manuscript. Generic Mapping Tools [Wessel and Smith, 1995] and Seismic Unix software package [Stockwell, 1999] were used in the preparation this manuscript.

References

- Archer, S. G., Bergman, S. C., Iliffe, J., Murphy, C. M., & Thornton, M. (2005). Palaeogene igneous rocks reveal new insights into the geodynamic evolution and petroleum potential of the Rockall Trough, NE Atlantic Margin. *Basin Research*, 17(1), 171-201. DOI: 10.1111/j.1365-2117.2005.00260.x
- Bayrakci, G., Minshull, T. A., Sawyer, D. S., Reston, T. J., Klaeschen, D., Papenberg, C., et al. (2016). Fault-controlled hydration of the upper mantle during continental rifting. *Nature Geoscience*, (March), 1–6. <http://doi.org/10.1038/ngeo2671>
- Brune, S., Heine, C., Pérez-Gussinyé, M., & Sobolev, S. V. (2014). Rift migration explains continental margin asymmetry and crustal hyper-extension. *Nature Communications*, 5. DOI: 10.1038/ncomms5014
- Brune, S., Williams, S. E., Butterworth, N. P., & Müller, R. D. (2016). Abrupt plate accelerations shape rifted continental margins. *Nature*, 1–4. <http://doi.org/10.1038/nature18319>

438 Calvès, G., Torvela, T., Huuse, M., and Dinkleman, M. G. (2012). New evidence for the origin of the Porcupine
 439 Median Volcanic Ridge: Early Cretaceous volcanism in the Porcupine Basin, Atlantic margin of
 440 Ireland. *Geochemistry, Geophysics, Geosystems*, 13(6).

441 Carlson, R. L., & Miller, D. J. (2003). Mantle wedge water contents estimated from seismic velocities in
 442 partially serpentinised peridotites. *Geophysical Research Letters*, 30, 12–15.
 443 <http://doi.org/10.1029/2002GL016600>

444 Christensen, N. I. (2004). Serpentinites, peridotites, and seismology. *International Geology Review*, 46(9),
 445 795-816.

446 Christensen, N. I., & Mooney, W. D. (1995). Seismic velocity structure and composition of the continental
 447 crust: A global view. *Journal of Geophysical Research*, 100, 9761. <http://doi.org/10.1029/95JB00259>

448 Davy, R. G., Minshull, T. A., Bayrakci, G., Bull, J. M., Klaeschen, D., Papenberg, C., et al. (2015). Continental
 449 hyperextension, mantle exhumation, and thin oceanic crust at the continent-ocean transition, West
 450 Iberia: New insights from wide-angle seismic. *Journal of Geophysical Research: Solid Earth*, 121,
 451 3177–3199. <http://doi.org/10.1002/2015JB012352>. Received

452 Funck, T., Hopper, J. R., Larsen, H. C., Loudon, K. E., Tucholke, B. E., & Holbrook, W. S. (2003). Crustal
 453 structure of the ocean-continent transition at Flemish Cap: Seismic refraction results. *Journal of*
 454 *Geophysical Research: Solid Earth*, 108(B11).

455 Escartín, J., Hirth, G., & Evans, B. (2001). Strength of slightly serpentinised peridotites: Implications for the
 456 tectonics of oceanic lithosphere. *Geology*, 29(11), 1023-1026.

457 Guillot, S., Schwartz, S., Reynard, B., Agard, P., & Prigent, C. (2015). Tectonic significance of serpentinites.
 458 *Tectonophysics*, 646, 1-19. <http://dx.doi.org/10.1016/j.tecto.2015.01.020>

459 Hughes, S., Barton, P., & Harrison, D. (1998). Exploration in the Shetland-Faeroe Basin using densely spaced
 460 arrays of ocean-bottom seismometers. *Geophysics*, 2, 490–501.

461 Huisman, R. S., and Beaumont, C. (2003). Symmetric and asymmetric lithospheric extension: Relative effects
 462 of frictional-plastic and viscous strain softening, *J. Geophys. Res.*, 108(B10), 2496,
 463 doi:10.1029/2002JB002026.

464 Johnson, H., J. Ritchie, R. Gatliff, J. Williamson, J. Cavill, and J. Bulat (2001), Aspects of the structure of the
 465 Porcupine and Porcupine Seabight basins as revealed from gravity modelling of regional seismic

466 transects, Geological Society, London, Special Publications, 188(1), 265-274.
 467 doi:10.1144/GSL.SP.2001.188.01.15

468 Klemper, S., and Hobbs, R., (1991). The BRIPS Atlas. Deep seismic reflection profiles around the British
 469 Isles. Cambridge University Press, Cambridge, pp. 124

470 Korenaga, J., Holbrook, W. S., Kent, G. M., Kelemen, P. B., Detrick, R. S., Larsen, H. C., Hopper, J. R. &
 471 Dahl-Jensen, T. (2000). Crustal structure of the southeast Greenland margin from joint refraction and
 472 reflection seismic tomography. *Journal of Geophysical Research - Solid Earth*, 105, 21591-21614,
 473 doi:10.1029/2000JB900188.

474 Korenaga, J., Holbrook, W. S., Detrick, R. S., & Kelemen, P. B. (2001). Gravity anomalies and crustal structure
 475 at the southeast Greenland margin. *Journal of Geophysical Research: Solid Earth*, 106, 8853-8870.

476 Lowe, C., and Jacob, A.W.B., (1989). A north-south seismic profile across the Caledonian suture zone in
 477 Ireland. *Tectonophysics* 168, 297–318.

478 Miller, N. C., and D. Lizarralde (2016), Finite-frequency wave propagation through outer rise fault zones and
 479 seismic measurements of upper mantle hydration, *Geophys. Res. Lett.*, 43, 7982–7990,
 480 doi:10.1002/2016GL070083.

481 Moore, D. E., Lockner, D. A., Summers, R., Shengli, M. A., & Byerlee, J. D. (1996). Strength of chrysotile-
 482 serpentinite gouge under hydrothermal conditions: Can it explain a weak San Andreas
 483 fault?. *Geology*, 24(11), 1041-1044.

484 Naylor, D., P. Shannon, & N. Murphy (2002), Porcupine-Goban Region: A Standard Structural Nomenclature
 485 System, Department of the Marine and Natural Resources, Petroleum Affairs Division.

486 Naylor, D. & Shannon, P.M. (2011). *Petroleum Geology of Ireland*. Dunedin Academic Press, Edinburgh,
 487 Scotland. pp.262.

488 O'Hanley, D. S. (1992). Solution to the volume problem in serpentinisation. *Geology*, 20, 705–708.

489 O'Reilly, B.M., Hauser, F., Jacob, A.W.B. & Shannon, P.M. (1996). The lithosphere below the Rockall
 490 Trough: wide-angle seismic evidence for extensive serpentinisation. *Tectonophysics*, 255, 1-23,
 491 doi:10.1016/0040-1951(95)00149-2.

492 O'Reilly, B.M., Hauser, F., Readman, P.W. (2010). The fine-scale structure of upper continental lithosphere
 493 from seismic waveform methods: insights into Phanerozoic crustal formation processes. *Geophysical*
 494 *Journal International* 180 (1), 101–124.

495 O'Reilly, B. M., Hauser, F., Ravaut, C., Shannon, P. M. & Readman, P. W. (2006). Crustal thinning, mantle
 496 exhumation and serpentinitisation in the Porcupine Basin, offshore Ireland: evidence from wide-angle
 497 seismic data. *Journal of the Geological Society, London*, 163, 775-787, doi:10.1144/0016-76492005-
 498 079.

499 Pérez-Gussinyé, M. & Reston, T. J. (2001). Rheological evolution during extension at nonvolcanic rifted
 500 margins: onset of serpentinitisation and development of detachments leading to continental breakup.
 501 *Journal of Geophysical Research - Solid Earth*, 106, 3961-3975, doi:10.1029/2000JB900325.

502 Pérez-Gussinyé, M., Morgan, J. P., Reston, T. J., & Ranero, C. R. (2006). The rift to drift transition at non-
 503 volcanic margins: Insights from numerical modelling. *Earth and Planetary Science Letters*, 244(1),
 504 458-473.

505 Ranero, C. R., J. P. Morgan, K. McIntosh, and C. Reichert (2003), Bending-related faulting and mantle
 506 serpentinitization at the Middle America trench, *Nature*, 425(6956), 367–373.

507 Readman, P. W., O'Reilly, B. M., Shannon, P. M. & Naylor, D. (2005). The deep structure of the Porcupine
 508 Basin, offshore Ireland, from gravity and magnetic studies. In *Geological Society, London, Petroleum*
 509 *Geology Conference series*, 6, 1047-1056, doi:10.1144/0061047.

510 Reid, I., & Jackson, H. R. (1981). Oceanic spreading rate and crustal thickness. *Marine Geophysical*
 511 *Researches*, 5(2), 165-172.

512 Reston, T. J., Pennell, J., Stubenrauch, A., Walker, I., & Perez-Gussinye, M. (2001). Detachment faulting,
 513 mantle serpentinitisation, and serpentinite-mud volcanism beneath the Porcupine Basin, southwest of
 514 Ireland. *Geology*, 29(7), 587-590.

515 Reston, T. J., Gaw, V., Pennell, J., Klaeschen, D., Stubenrauch, A. & Walker, I. (2004). Extreme crustal
 516 thinning in the south Porcupine Basin and the nature of the Porcupine Median High: implications for
 517 the formation of non-volcanic rifted margins. *Journal of the Geological Society*, 161(5), 783-798,
 518 doi:10.1144/0016-764903-036.

519 Reston, T. J., Leythaeuser, T., Booth-Rea, G., Sawyer, D., Klaeschen, D., & Long, C. (2007). Movement along
 520 a low-angle normal fault: The S reflector west of Spain. *Geochemistry, Geophysics, Geosystems*, 8,
 521 n/a-n/a. <http://doi.org/10.1029/2006GC001437>

522 Sallarès, V., Gailler, A., Gutscher, M. A., Graindorge, D., Bartolomé, R., Gracia, E., Díaz, J., Dañobeitia, J.J.
 523 & Zitellini, N. (2011). Seismic evidence for the presence of Jurassic oceanic crust in the central Gulf

524 of Cadiz (SW Iberian margin). *Earth and Planetary Science Letter*, 311, 112-123,
525 doi:10.1016/j.epsl.2011.09.003.

526 Sandwell, D. T., R. D. Müller, W. H. F. Smith, E. Garcia, R. Francis, (2014) New global marine gravity model
527 from CryoSat-2 and Jason-1 reveals buried tectonic structure, *Science*, Vol. 346, no. 6205, pp. 65-67,
528 doi:10.1126/science.1258213

529 Stockwell, J. W. (1999), The CWP/SU: Seismic unix package, *Comput.Geosci.*, 25(4), 415–419.

530 Tarantola, A., (1987). *Inverse problem theory: methods for data fitting and model parameter estimation*.
531 Elsevier Science, New York 613

532 Tate, M. P., White, N. & Conroy, J.-J. (1993). Lithospheric extension and magmatism in the Porcupine Basin
533 west of Ireland. *Journal of Geophysical Research - Solid Earth*, 98, 13905-13923,
534 doi:10.1029/93JB00890.

535 Tate, M. P. & Dobson, M. R. (1988). Syn-and post-rift igneous activity in the Porcupine Seabight Basin and
536 adjacent continental margin W of Ireland. *Geological Society, London, Special Publications*, 39, 309-
537 334, doi:10.1144/GSL.SP.1988.039.01.28.

538 Tutolo, B. M., Mildner, D. F., Gagnon, C. V., Saar, M. O., & Seyfried, W. E. (2016). Nanoscale constraints
539 on porosity generation and fluid flow during serpentinisation. *Geology*, 44(2), 103-106.

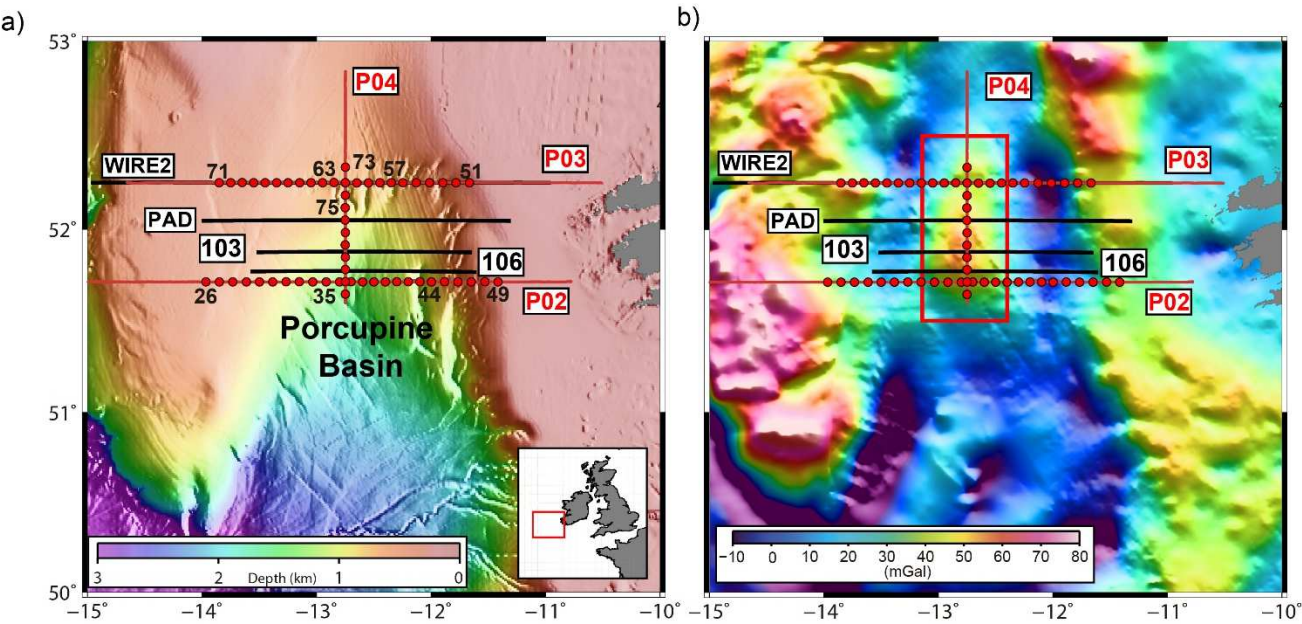
540 Watremez, L., Prada, M., Minshull, T., O'Reilly, B., Chen, C., Reston, T., Shannon, P., Wagner, G., Gaw, V.,
541 Klaeschen, D., Edwards, R., and Lebedev, S., (2016). Deep structure of the Porcupine Basin from
542 wide-angle seismic data. *Geological Society, London, 8th Petroleum Geology Conference*
543 *Proceedings*. doi:10.1144/PGC8.26

544 Weatherall P., K. M. Marks, M. Jakobsson, T. Schmitt, S. Tani, J. E. Arndt, M. Rovere, D. Chayes, V. Ferrini,
545 and R. Wigley (2015), A new digital bathymetric model of the world's oceans, *Earth and Space*
546 *Science*, 2, 331–345, doi: 10.1002/2015EA000107.

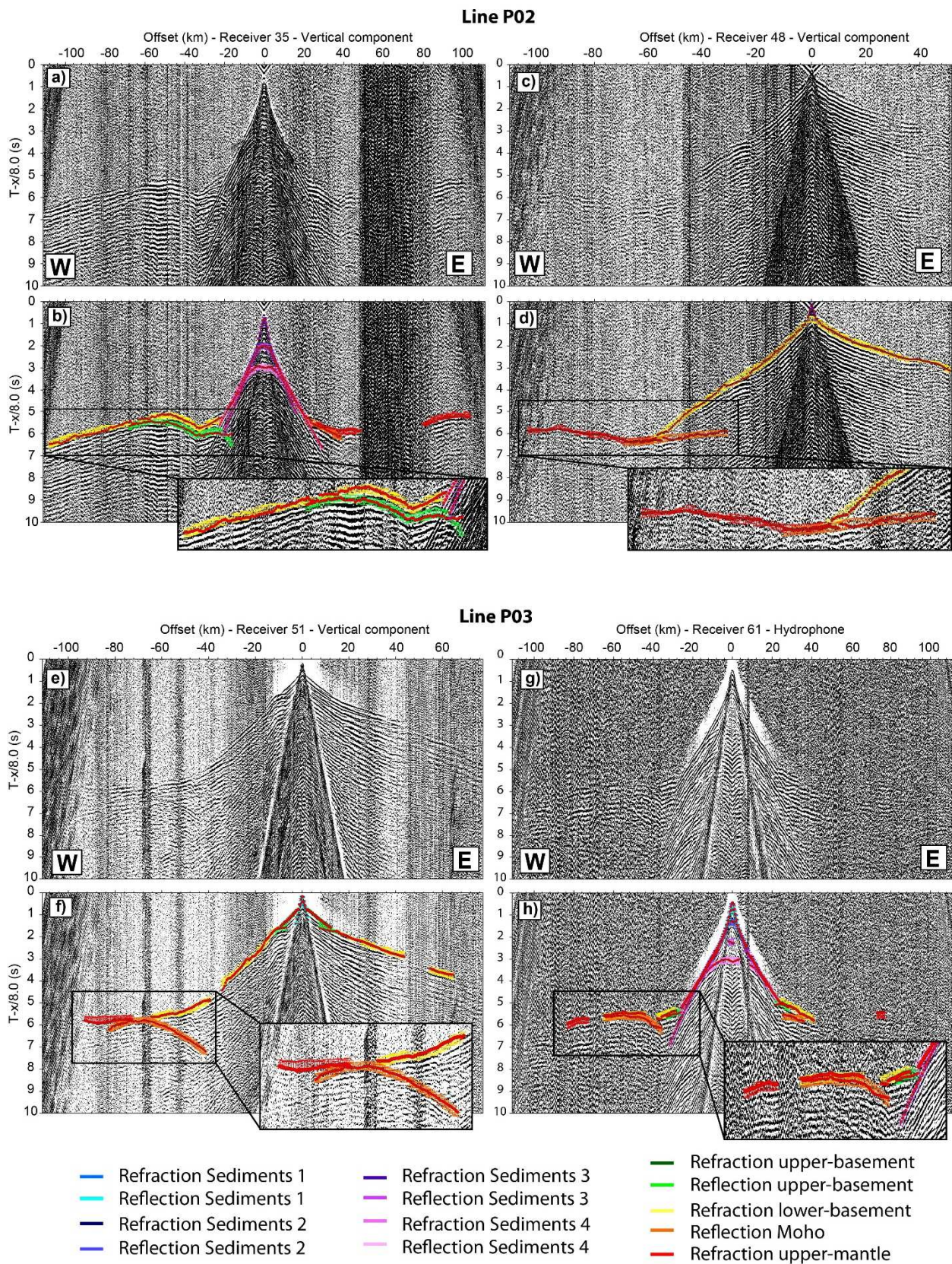
547 Wessel, P. & Smith, W. H. (1998). New, improved version of Generic Mapping Tools released. *Eos*,
548 *Transactions American Geophysical Union*, 79, 579-579, doi:10.1029/98EO00426

549 Whitmarsh, R. B., White, R. S., Horsefield, S. J., Sibuet, J. C., Recq, M., & Louvel, V. (1996). The ocean-
550 continent boundary off the western continental margin of Iberia: Crustal structure west of Galicia
551 Bank. *Journal of Geophysical Research: Solid Earth*, 101(B12), 28291-28314.

552 Zelt, C. A., & Forsyth, D. A. 1994. Modeling wide-angle seismic data for crustal structure: Southeastern
553 Grenville Province. *Journal of Geophysical Research - Solid Earth*, 99, 11687-11704,
554 doi:10.1029/93JB02764.



556 **Figure 1.-** (a) Bathymetry of the Porcupine Basin, southwest of Ireland (see inset), depicting the
557 location of wide-angle seismic lines (red lines) and seismic reflection lines (black lines) used in this
558 study. Wire2 was presented by *Klemper and Hobbs [1991]*. Seismic reflection lines 103 and 106 were
559 previously presented by *Reston et al. [2001, 2004]*. Red circles are ocean-bottom receivers used to
560 acquire wide-angle seismic data. Bathymetry data set is from *Weatherall et al. [2015]*. (b) Free air
561 gravity anomaly map of the Porcupine Basin obtained from satellite data [*Sandwell et al., 2014*]. The
562 red rectangle highlights the area of the gravity anomaly related to the Porcupine Arch.
563



564

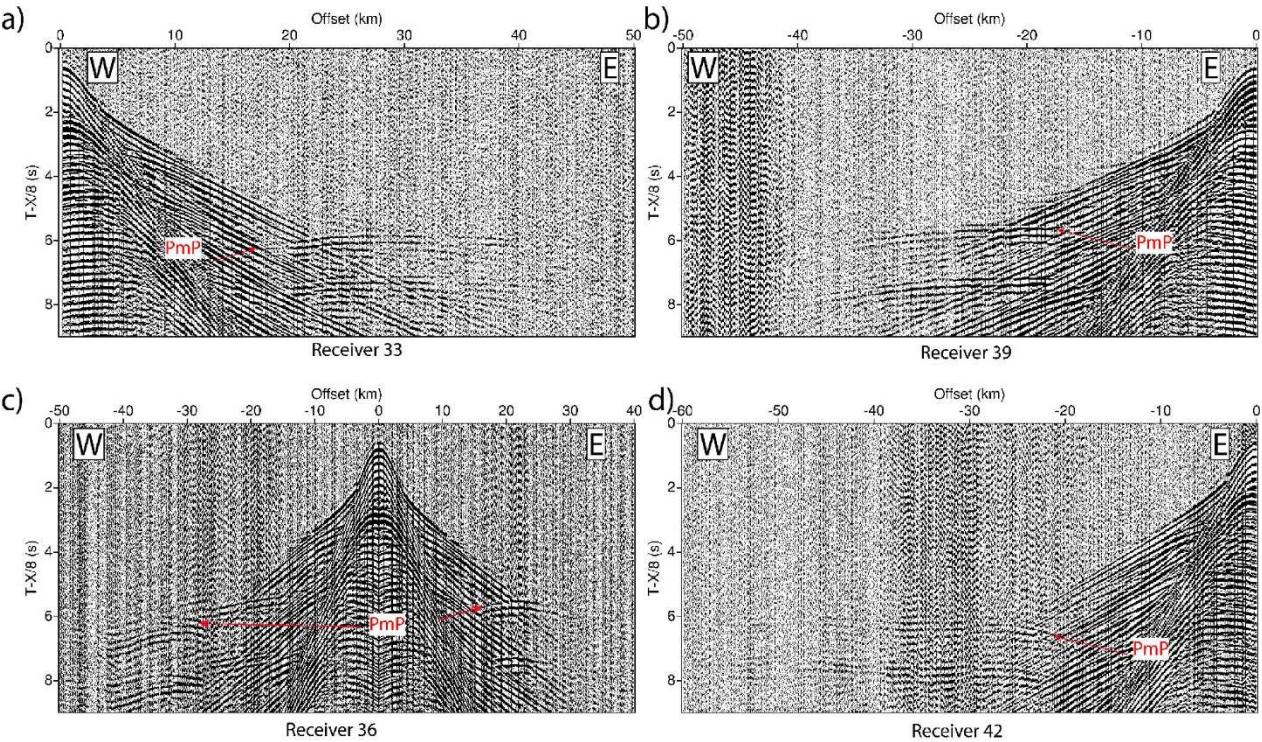
565

566

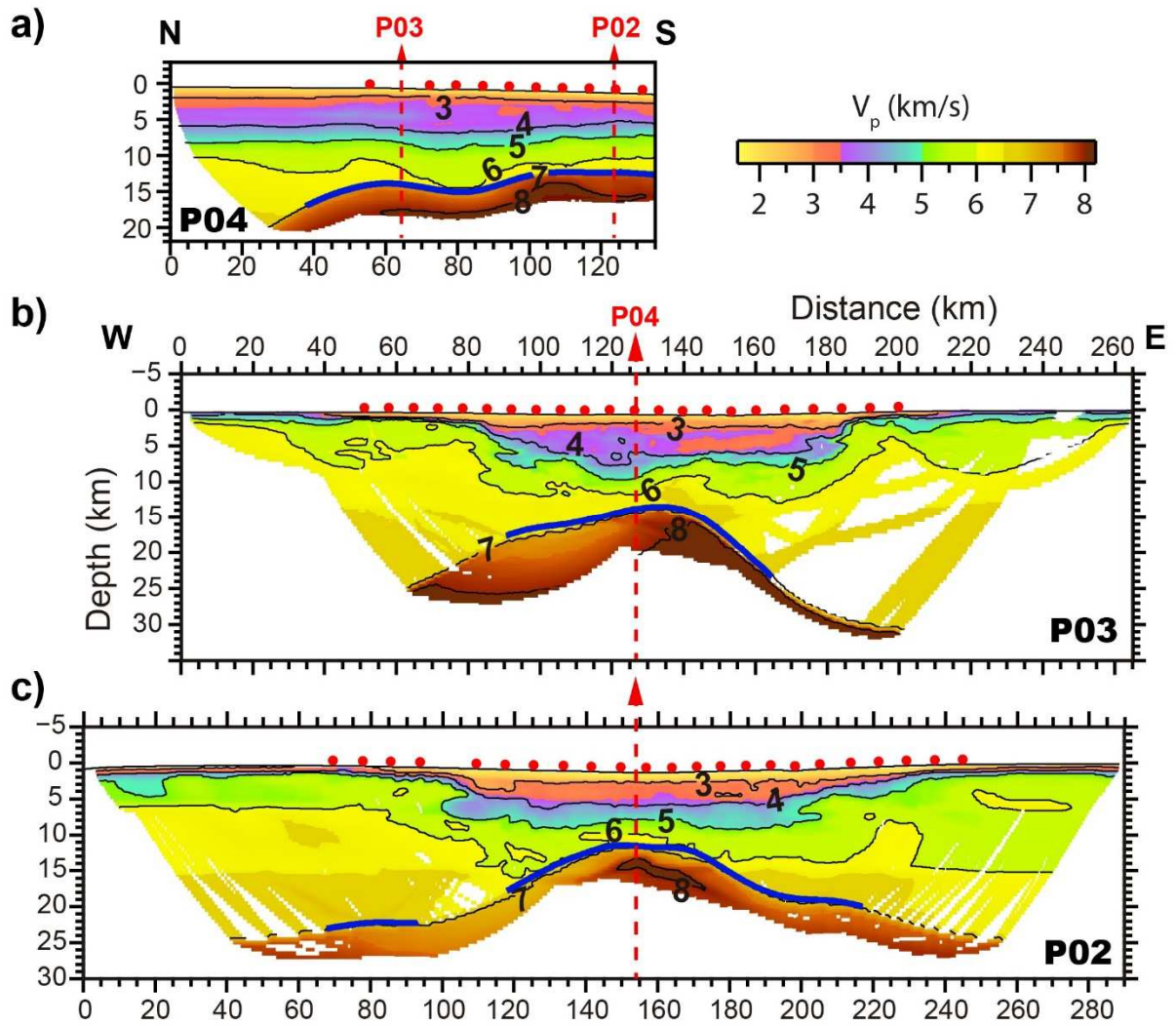
567

Figure 2.- Record sections of the vertical component of OBS 35 (a, b) and 48 (c, d) along P02, and OBS 51 (e, f) and hydrophone 61 (g, h) along P03. Panels b, d f, and h show observed seismic phases (coloured error bars), and calculated travel times (red dots). Record sections are reduced at 8 km/s.

568 Reflected sedimentary seismic phases were used to invert for those sedimentary interfaces shown in
569 Fig. A1.



570
571 **Figure 3.-** Close up of record sections from **hydrophone** 33 (a), 39 (b), 36 (c) and 42 (d) along P02,
572 showing critical reflected phases interpreted as P_mP . Note that all record sections are reduced in time
573 using a velocity of 8 km/s.



574

575 **Figure 4.-** (a) P-wave velocity (V_p) model P04 (strike line), (b) P03 and (c) P02 (dip lines). Seismic
576 velocities are shown where the derivative weight sum is > 0 (see Fig. A3 for more information on the
577 derivative weight sum). **Note that the uppermost mantle is well covered by rays in the area of interest**
578 **for the study (i.e. the basin centre).** Blue line is the P_mP -derived Moho (see Fig. A4 for ray tracing of
579 P_mP arrivals). Red dots are ocean-bottom seismometers/hydrophones.

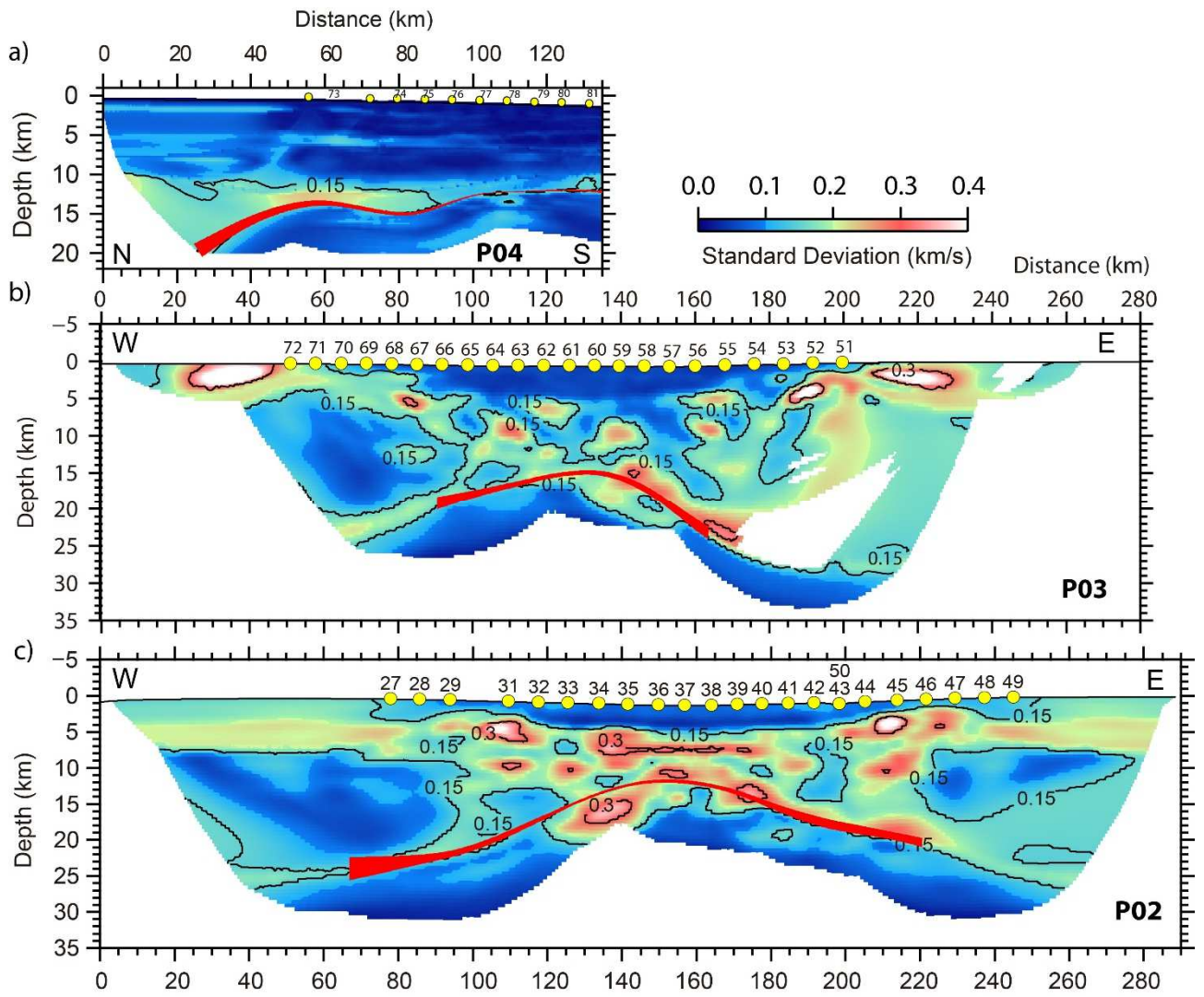
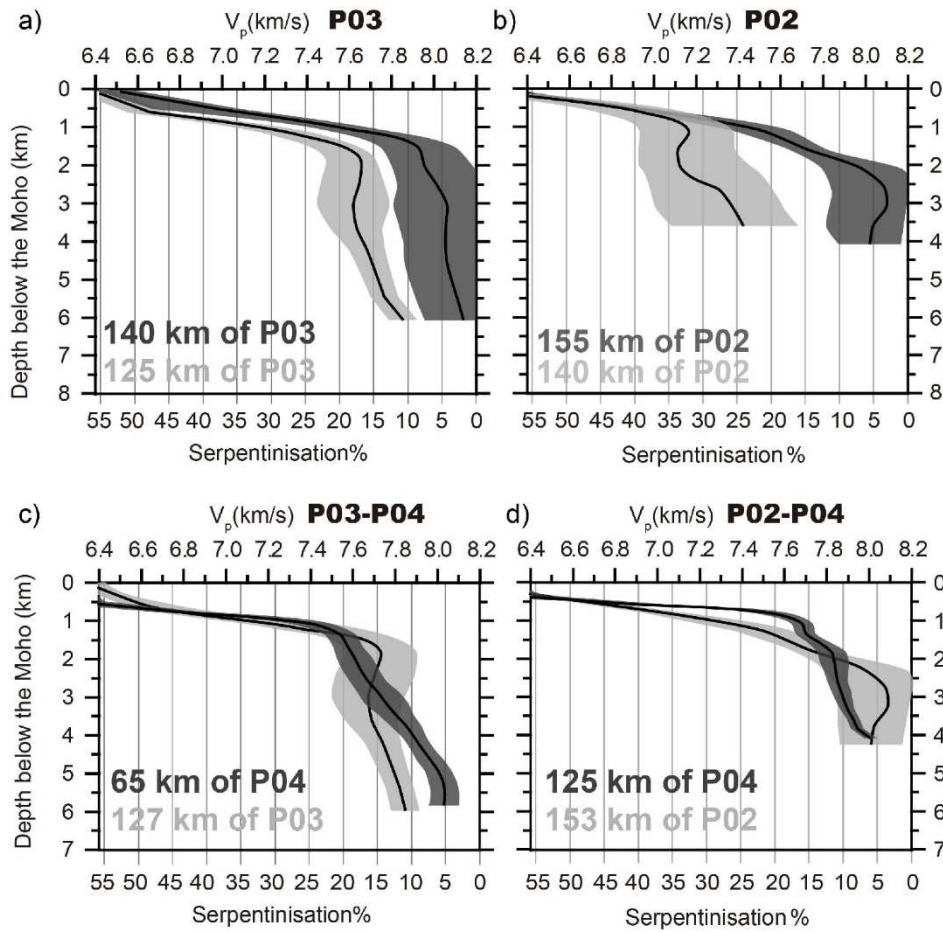
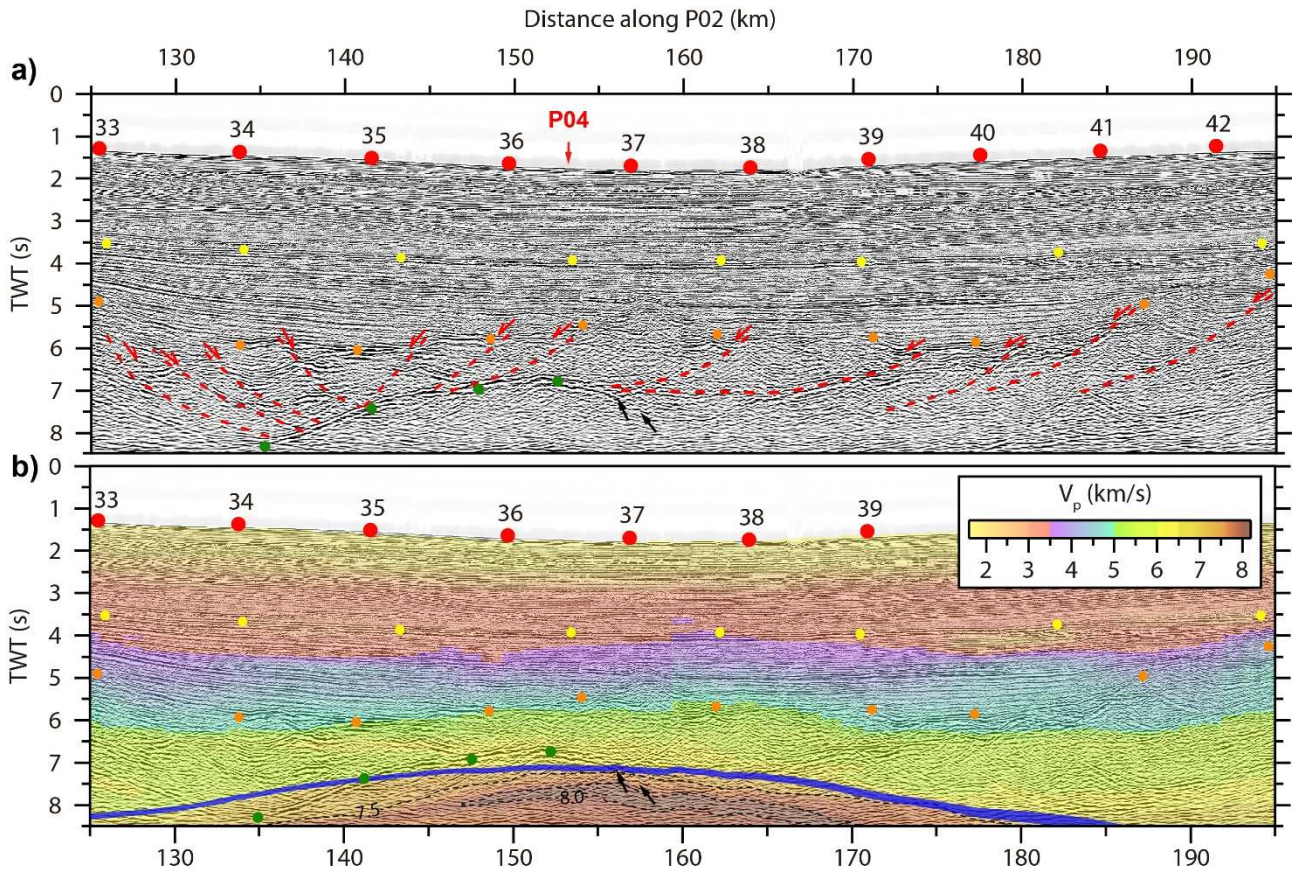


Figure 5.- Standard deviation of V_p values of the average solution of the Monte-Carlo analysis for profiles P04 (a), P03 (b), and P02 (c). The width of the red band shows the standard deviation of the depth of the Moho.



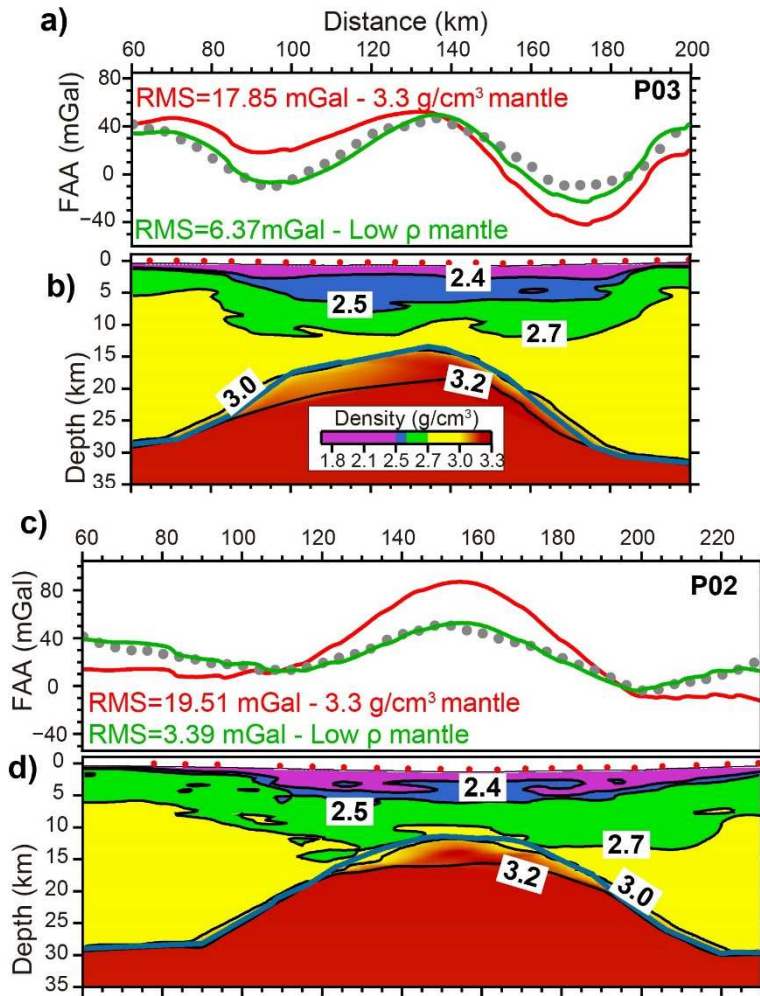
584

585 **Figure 6.-** 1D V_p vs depth diagrams of the uppermost mantle of models P03 (a) and P02 (b) showing
586 across-axis variations in mantle V_p . The degree of serpentinisation is derived from V_p using the
587 empirical relationship of *Carlson and Miller [2003]*, assuming a V_p of 8.2 km/s for unaltered
588 peridotite (i.e. 0% serpentinisation). The grey area represents the standard deviation computed from
589 the Monte-Carlo analysis, and the black solid lines are the vertical velocity structure extracted from
590 models in Fig. 4 at the profile distance given in the figure. We interpret the steep velocity gradient
591 ($\sim 1 \text{ s}^{-1}$) in the first 2 km of each profile as a partially serpentinised, tectonically-controlled shear zone
592 between the crust and mantle, whereas the gentle gradient below ($\sim 0.1 \text{ s}^{-1}$) suggests a change to a less
593 pervasively deformed but still fractured zone with less serpentinisation. (c) and (d) are 1D V_p vs depth
594 diagrams comparing the seismic structure of profiles P03 and P02 with that of P04 at the intersection
595 point between models.



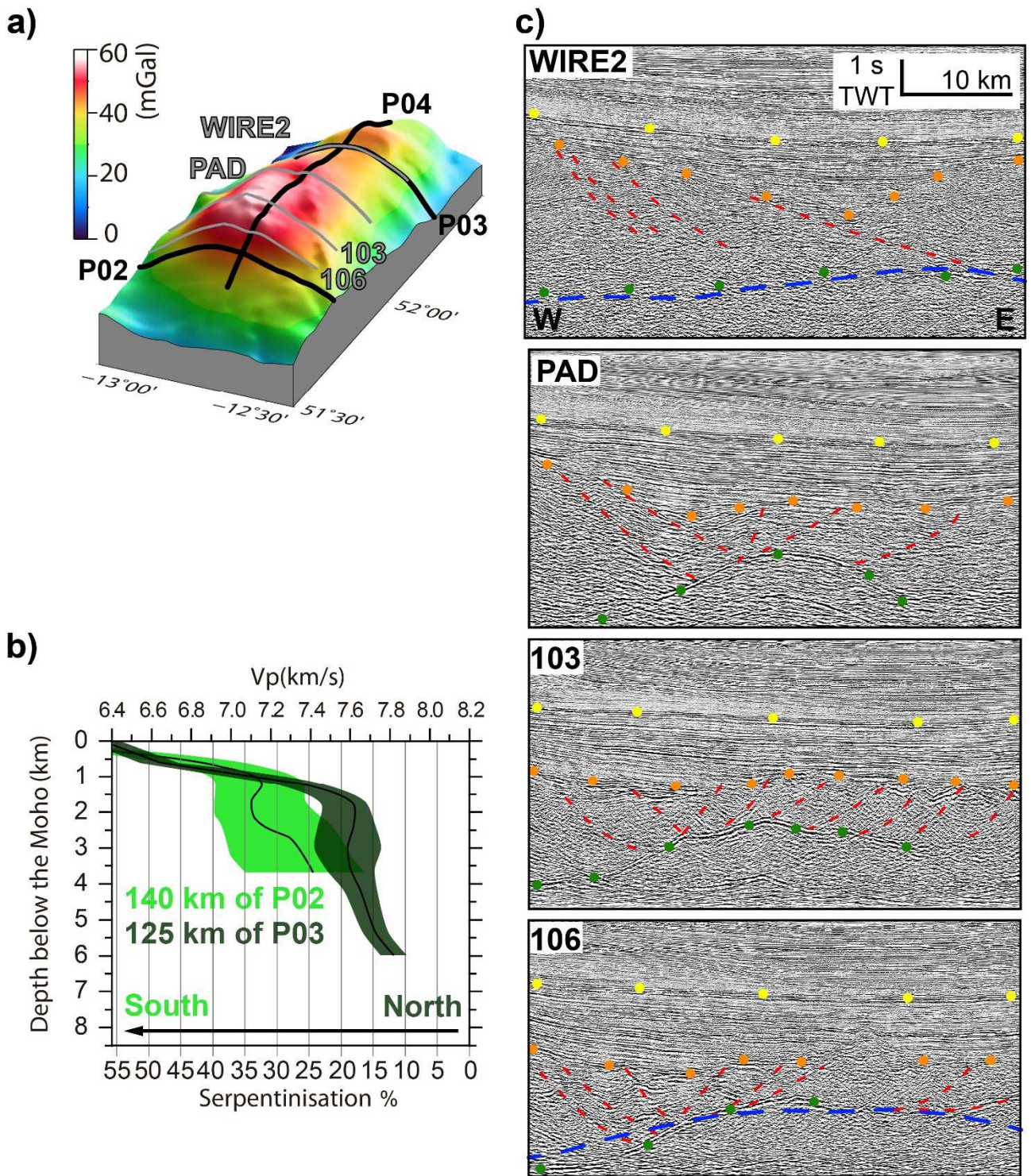
596

597 **Figure 7.- (a)** Time-migrated seismic reflection line 106 showing crustal faults modified from [Reston](#)
 598 [et al. \[2004\]](#). Red dots are OBS/H, while yellow and orange dots depict the top of the Cretaceous unit
 599 and top of the syn-rift sequence, respectively. Green dots follow the P-detachment reflectivity there
 600 where it corresponds to the Moho. Black arrows show the eastward dipping reflectivity interpreted as
 601 the Moho by [Reston et al. \[2001\]](#). **Black arrows also depict the location where the P-detachment**
 602 **diverges from the Moho and becomes an intracrustal feature (see Fig. 2 in Reston et al., 2001).** TWT:
 603 two-way time **(b)** Time-migrated seismic reflection line 106 overlaid by seismic velocities of model
 604 P02 converted from depth to two-way time assuming a near-vertical propagation. The width of the
 605 blue band shows the standard deviation of the depth of the WAS-derived Moho calculated in the
 606 Monte-Carlo analysis. See section 5.1 for detailed discussion on the mismatch between the WAS-
 607 derived Moho and the MCS-interpreted Moho observed along this image.



608

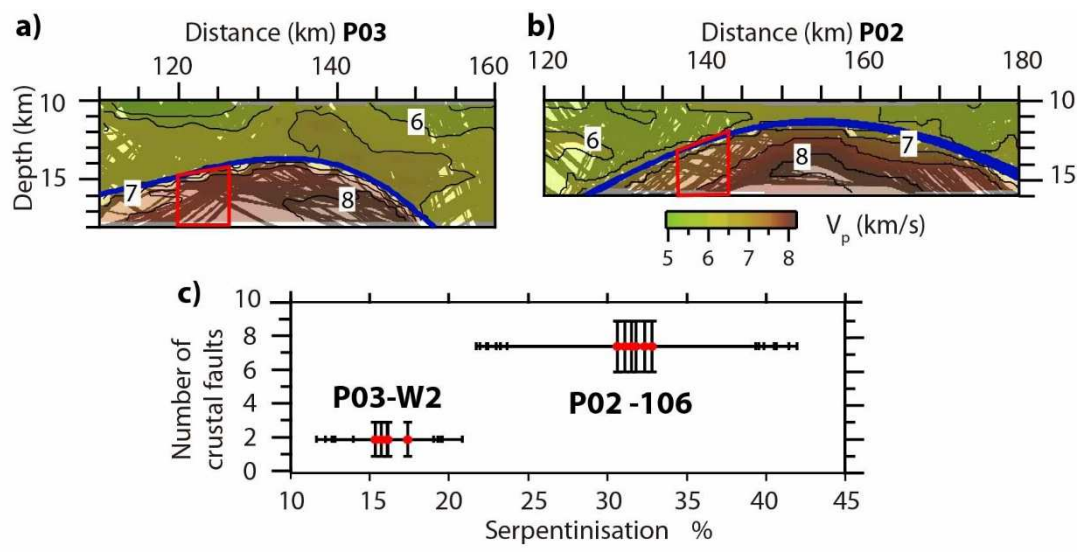
609 **Figure 8.-** (a) Observed free air gravity anomaly (FAA) from satellite measurements [Sandwell *et*
610 *al.*, 2014] (white circles) and synthetic anomaly (red & green lines) obtained along line P03. (b)
611 Density model used to compute the best-fitted synthetic anomaly along P03 (green line). The Moho
612 (blue line) has been extracted from velocity models in Fig. 4, and modified in the margins, where P_mP
613 ray coverage was poor. The red line was obtained using the same density model as in (b) but with a
614 3.3 g/cm³ homogeneous mantle density. (c) and (d) correspond to the same as (a) and (b), respectively,
615 but along line P02. These results show that across-axis variations in mantle density are required to
616 explain the gravity anomaly, and therefore support across-axis variations in the degree of
617 serpentinisation.



618

619 **Figure 9.-** (a) 3D view of the gravity anomaly highlighted in Fig. 1b. Thick black lines depict the
 620 location of WAS lines, whereas thin grey lines show the location of reflection lines used in this study.
 621 (b) 1D V_p vs depth diagrams of the upper mantle of models P02 and P03 showing how upper mantle
 622 V_p decreases southwards, suggesting an increasing degree of serpentinisation. The shaded areas show
 623 the standard deviations computed from the Monte-Carlo analysis. (c) From top (north) to bottom
 624 (south), time-migrated seismic reflection lines Wire2, PAD, 103 and 106, showing the increment of
 625 crustal faulting (dashed red lines) and variations of the P-detachment surface (green circles) along the
 626 basin axis. Blue dashed line is the Moho derived from WAS data. Orange dots depict top of syn-rift,

627 while yellow dots show top Cretaceous. Wire2 was previously discussed by *Klemper and Hobbs*
 628 *[1991]* and *Watremez et al. [2016]*.

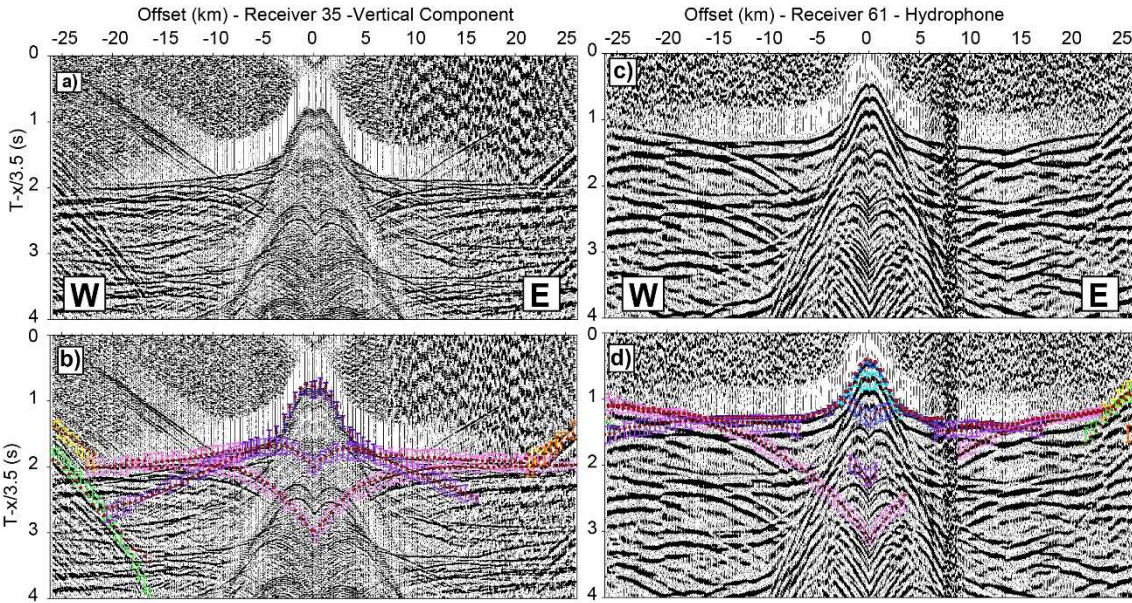


629
 630 **Figure 10.- (a, b)** Ray coverage of the lower crust and uppermost mantle along lines P03 and P02,
 631 respectively. The width of the blue band shows the standard deviation of the depth of the Moho, while
 632 the red box depicts the region chosen to derive the vertically averaged degree of serpentinisation
 633 shown in (d). **These areas are selected because they are constrained by comparatively high ray**
 634 **coverage, and because they are located beneath crustal faulting potentially responsible for mantle**
 635 **hydration.** (c) Vertically averaged V_p -derived degree of serpentinisation from the red box in (b) and
 636 (c) vs the number of crustal faults interpreted from seismic reflection lines Wire2 (coincident to P03)
 637 and 106 (neighbour to P02). The degree of serpentinisation was derived from V_p using the empirical
 638 relationship of *Carlson and Miller [2003]*. The interpreted amount of faulting is displayed within a
 639 range of uncertainty based on observations from seismic lines in Fig. 9c. The uncertainty of the degree
 640 of serpentinisation is derived from results of the Monte-Carlo analysis in Fig. 5.

641

642 Figures A1 to A4 provide information about the layer stripping sequence followed to obtain the
 643 tomographic models P04, P02, and P03, as well as ray tracing information of each model. Tables A1
 644 to A3 contain information regarding modelling statistics of each tomographic model.

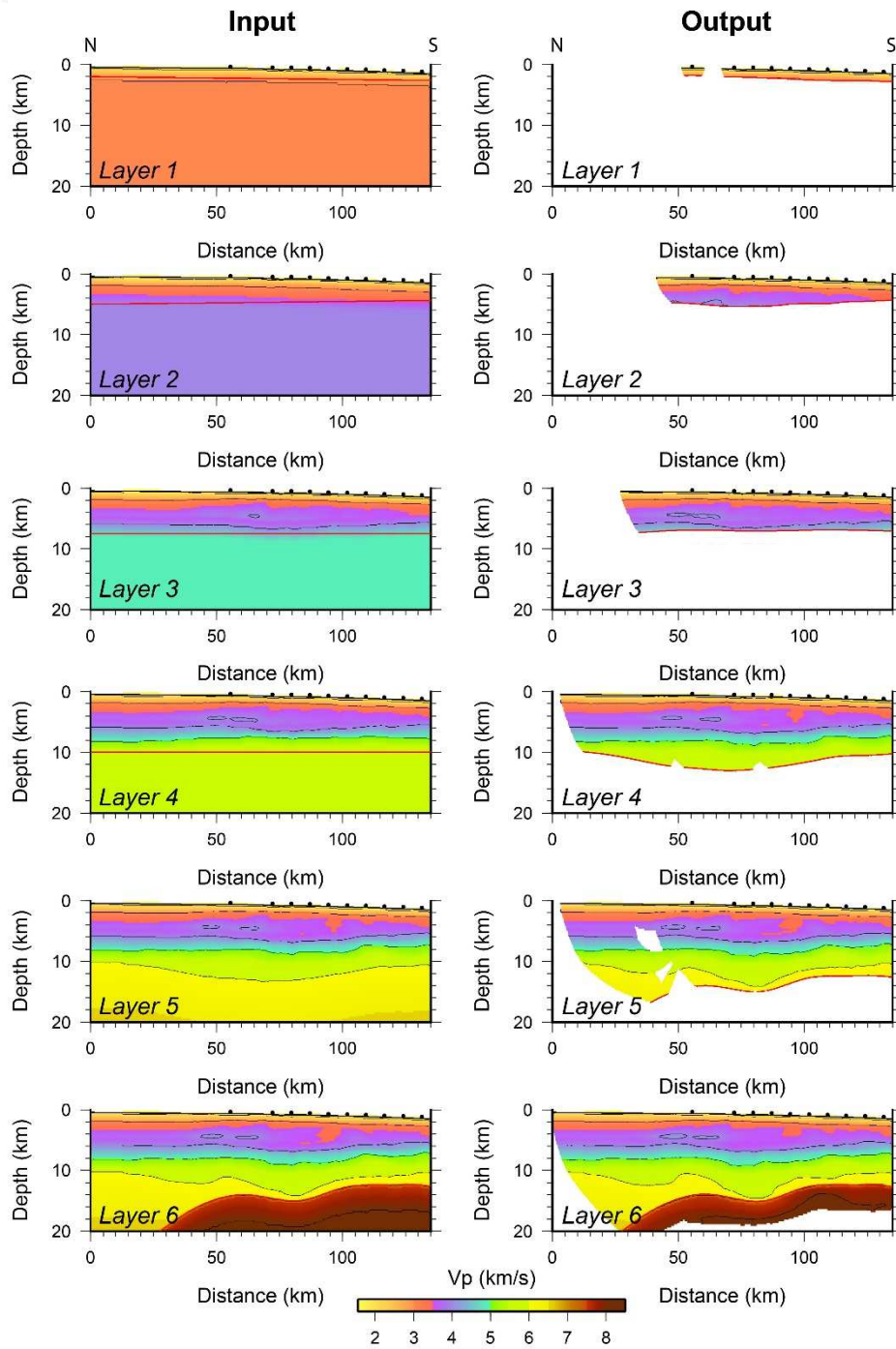
645



646

647 **Figure A1.-** Close up of record sections of the vertical component of OBS 35 (**a, b**) along P02, and
 648 hydrophone 61 (**c, d**) along P03. Panels **b, d** show observed seismic phases (coloured error bars, see
 649 Fig. 2 for colour code), and calculated travel times (red dots). Record sections are reduced at 3.5 km/s.
 650 Reflected sedimentary seismic phases were used to invert for those sedimentary interfaces shown in
 651 Fig. A2.

a)



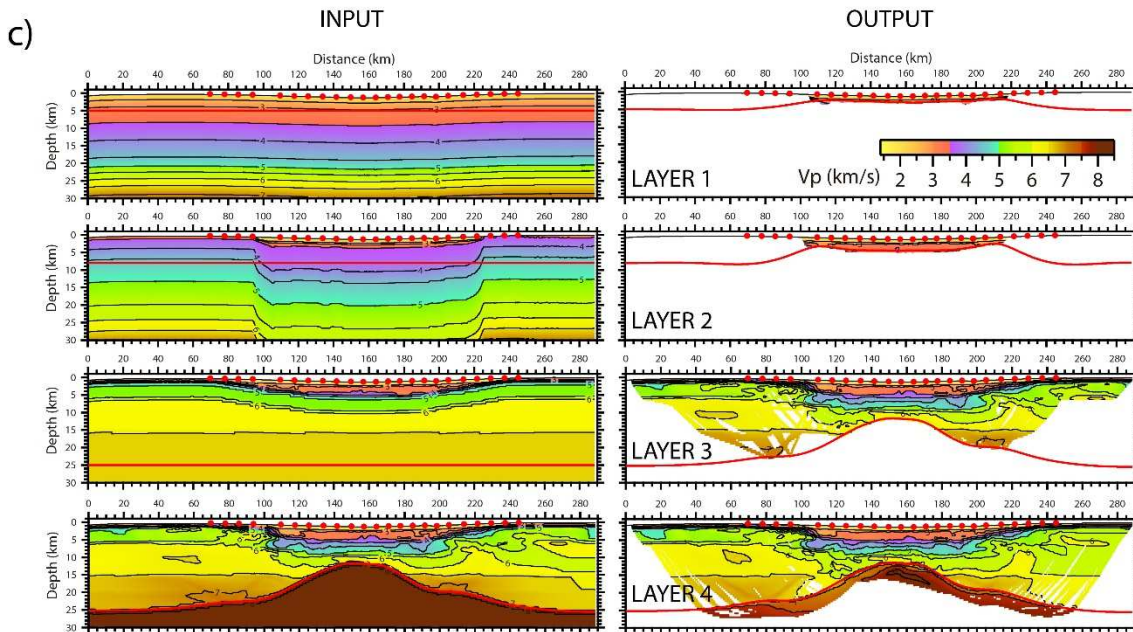
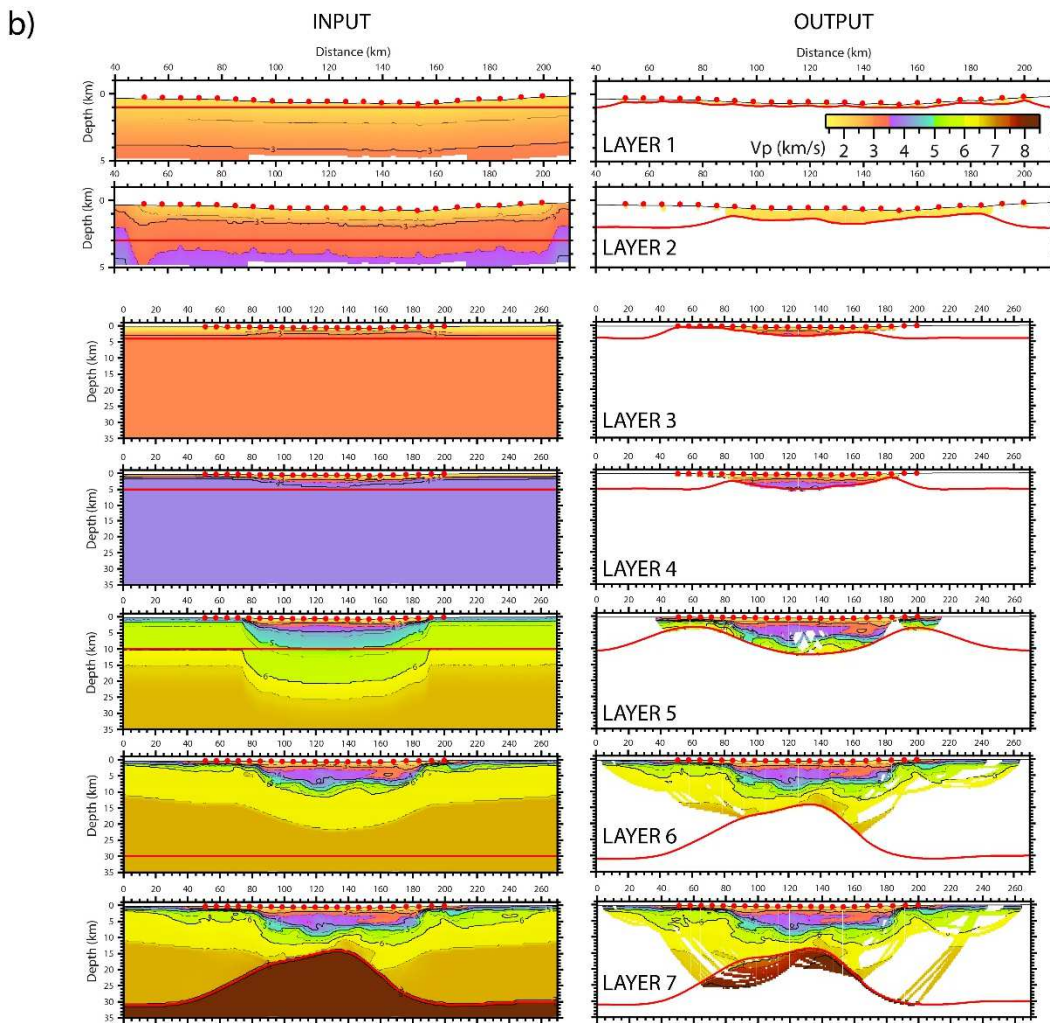


Figure A2.- Layer stripping sequence of models P04 (a), P03 (b) and P02 (c). This sequence illustrates the construction of each model. Examples of travel times used to invert for sedimentary interfaces are shown in Fig. 2.

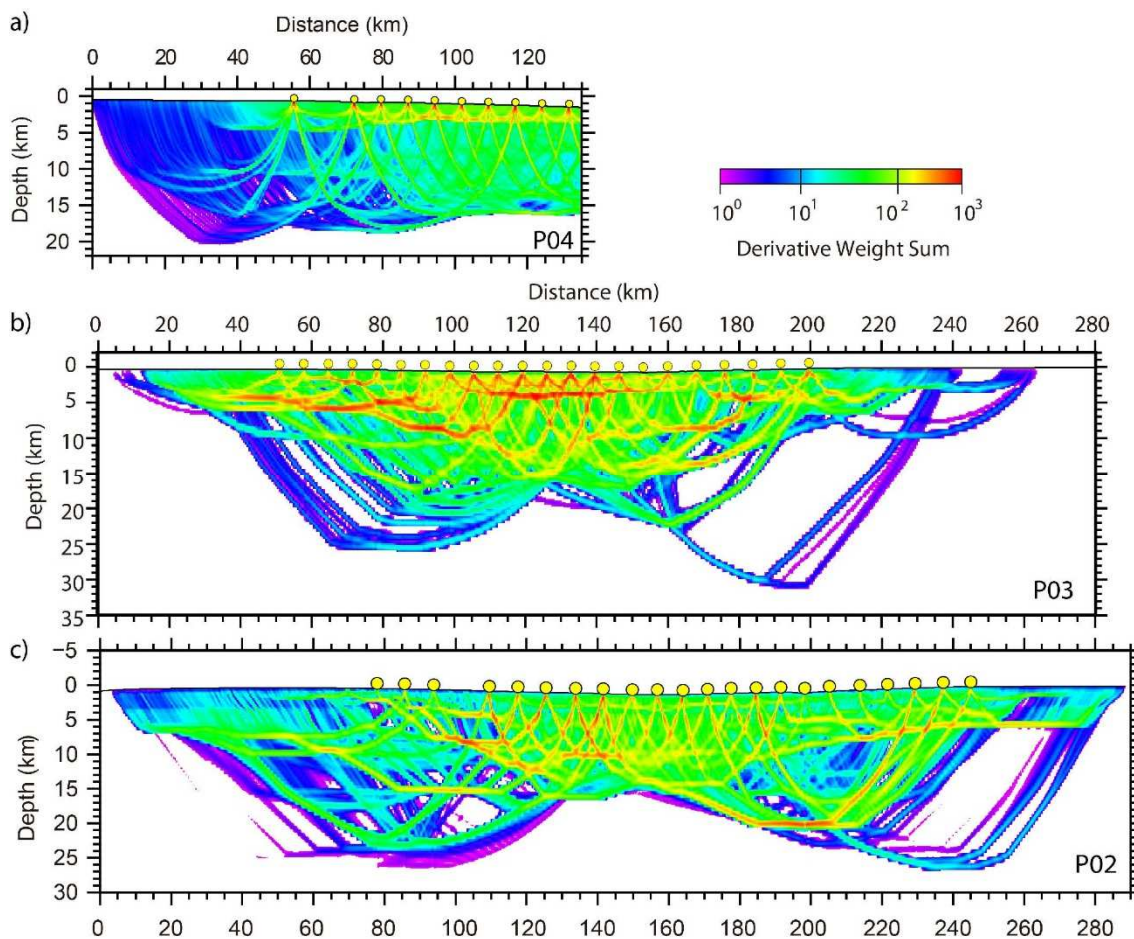
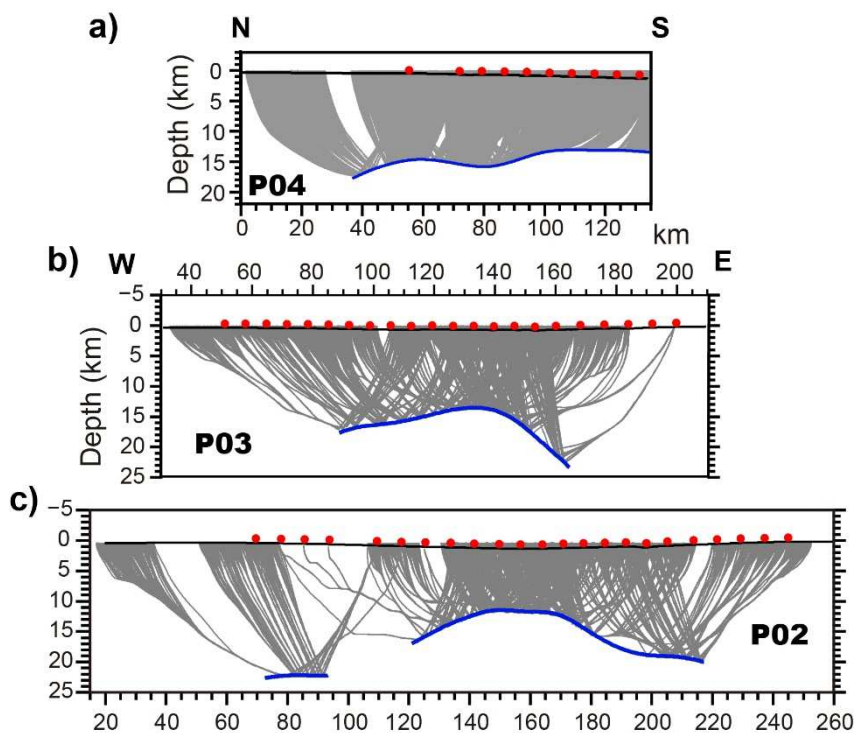


Figure A3.- Derivative weight sum of profiles P04 (a), P03 (b) and P02 (c). These images provide a quantitative estimate of the ray density along this line



663 **Figure A4.-** Ray tracing of P_mP arrival times of WAS profiles P04 (a), P03 (b) and P02 (c). Blue
664 thick line shows the inverted geometry of the Moho, whereas red dots are ocean-bottom receivers.
665 Black line depicts the seafloor topography.
666

Table A1. Modelling statistics for P02. The “refr” (refractions), “refl” (reflections)” and “all” subscripts refer to the parts of dataset considered.

Step	Iteration*	N _{refr} †	N _{refl} †	t _{RMS-refr} ‡	t _{RMS-refl} ‡	t _{RMS-all} ‡	χ ² _{refr} §	χ ² _{refl} §	χ ² _{all} §
1	12	1,658	2,404	85	48	68	1.09	0.60	0.80
2	14	3,990	4,782	55	66	61	0.35	0.90	0.67
3	14	14,475	3,316	76	60	73	0.79	0.94	0.82
4	14	18,493	3,316	75	69	74	1.00	1.06	1.01

667 *Iteration chosen to build the input model of next step (or final model for step 6).

668 †Numbers of picks used for the modelling.

669 ‡Root mean squared travel-time residuals, in milliseconds.

670 §Normalised chi-squared.

671

Table A2. Modelling statistics for P03. The “refr” (refractions), “refl” (reflections)” and “all” subscripts refer to the parts of dataset considered.

Step	Iteration*	N _{refr} †	N _{refl} †	t _{RMS-refr} ‡	t _{RMS-refl} ‡	t _{RMS-all} ‡	χ ² _{refr} §	χ ² _{refl} §	χ ² _{all} §
1	4	654	1,050	32	31	32	1.18	0.22	0.58
2	9	978	886	25	32	28	0.82	0.13	0.49
3	9	2,399	3,445	20	38	32	0.48	0.25	0.35
4	9	4,410	4,124	17	29	23	0.29	0.12	0.21
5	9	5,955	1,819	36	83	51	0.98	1.04	0.99
6	4	15,580	3,004	58	95	65	0.60	1.11	0.69
7	4	17,348	3,004	61	84	65	0.62	0.91	0.66

672 *Iteration chosen to build the input model of next step (or final model for step 6).

673 †Numbers of picks used for the modelling.

674 ‡Root mean squared travel-time residuals, in milliseconds.

675 §Normalised chi-squared.

Table A3. Modelling statistics for P04. The “refr” (refractions), “refl” (reflections)” and “all” subscripts refer to the parts of dataset considered.

Step	Iteration*	N _{refr} †	N _{refl} †	t _{RMS-refr} ‡	t _{RMS-refl} ‡	t _{RMS-all} ‡	χ ² _{refr} §	χ ² _{refl} §	χ ² _{all} §
1	2	1,515	1,507	11	22	17	0.28	0.28	0.28
2	2	4,634	5,159	14	30	24	0.19	0.41	0.30
3	2	5,252	2,676	20	52	34	0.19	0.83	0.41
4	2	8,979	4,658	38	67	50	0.29	0.81	0.47
5	2	8,979	5,241	33	50	40	0.23	0.39	0.29
6	1	16,467	5,241	63	49	60	0.45	0.39	0.44

*Iteration chosen to build the input model of next step (or final model for step 6).

†Numbers of picks used for the modelling.

‡Root mean squared travel-time residuals, in milliseconds.

§Normalised chi-squared.

677
678
679
680
681
682
683